

AD

AD-E402 825

Technical Report ARWEC-TR-97014

**ANALYSIS OF AEROSOLS PRODUCED DURING TESTS OF
TUNGSTEN ALLOY KINETIC ENERGY PENETRATORS**

Dr. Kenneth Gold

October 1997



US ARMY
TANK AUTOMOTIVE AND
ARMAMENTS COMMAND
ARMAMENT RDE CENTER

**U.S. ARMY ARMAMENT RESEARCH, DEVELOPMENT AND
ENGINEERING CENTER**

Warheads, Energetics & Combat-support Armaments Center

Picatinny Arsenal, New Jersey

Approved for public release; distribution is unlimited.

DTIC QUALITY INSPECTED 3

19971121 014

The views, opinions, and/or findings contained in this report are those of the authors(s) and should not be construed as an official Department of the Army position, policy, or decision, unless so designated by other documentation.

The citation in this report of the names of commercial firms or commercially available products or services does not constitute official endorsement by or approval of the U.S. Government.

Destroy this report when no longer needed by any method that will prevent disclosure of its contents or reconstruction of the document. Do not return to the originator.

REPORT DOCUMENTATION PAGE

Form Approved
OMB No. 0704-0188

Public reporting burden for this collection of information is estimated to average 1 hour per response, including the time for reviewing instructions, searching existing data sources, gathering and maintaining the data needed, and completing and reviewing the collection of information. Send comments regarding this burden estimate or any other aspect of this collection of information, including suggestions for reducing this burden to Washington Headquarters Services, Directorate for Information Operations and Reports, 1215 Jefferson Davis Highway, Suite 1204, Arlington, VA 2202-4302, and to the Office of Management and Budget, Paperwork Reduction Project (0704-0188), Washington, DC 20503.

1. AGENCY USE ONLY (Leave Blank) 2. REPORT DATE
October 1997 3. REPORT TYPE AND DATES COVERED

4. TITLE AND SUBTITLE
ANALYSIS OF AEROSOLS PRODUCED DURING TESTS OF TUNGSTEN ALLOY KINETIC ENERGY PENETRATORS

5. FUNDING NUMBERS

6. AUTHOR(S)
Dr. Kenneth Gold

7. PERFORMING ORGANIZATION NAME(S) AND ADDRESS(ES)
ARDEC, WECAC
System Readiness Center (AMSTA-AR-WES)
Picatinny Arsenal, NJ 07806-5000

10. PERFORMING ORGANIZATION REPORT NUMBER

10. SPONSORING/MONITORING AGENCY NAME(S) AND ADDRESS(ES)
ARDEC, WECAC
Information Research Center (AMSTA-AR-WEL-TL)
Picatinny Arsenal, NJ 07806-5000

10. SPONSORING/MONITORING AGENCY REPORT NUMBER

Technical Report
ARWEC-TR-97014

11. SUPPLEMENTARY NOTES

12a. DISTRIBUTION/AVAILABILITY STATEMENT
Approved for public release; distribution is unlimited.

12b. DISTRIBUTION CODE

13. ABSTRACT
Kinetic energy (KE) penetrators made with tungsten alloys have historically been assumed to be relatively benign and to pose no health or environmental risks. No actual test data has ever been recorded to support this assumption. The assumption is based on the belief that, though a heavy metal, the tungsten constituent of the alloy is non-toxic. However, the presence of two toxic metals, nickel and cobalt, although in relatively small proportions, raises issues about the possible risks that may be associated with (a) inhalation of aerosols and (b) ingestion of the metals once they are introduced into the food chain.

This study was designed to characterize the sizes and shapes of tungsten alloy aerosol particles and fragments ejected from penetration tunnels during performance tests of KE penetrators. Special attention was directed to the elemental composition of particles in the respirable size range, the fraction of the aerosol most likely to reach the gas exchange region in the lungs. Dust particles and fragments were also examined in anticipation of performing solubility tests on the residues.

14. SUBJECT TERMS
Kinetic energy penetrators X-ray energy dispersive spectrometry
Scanning electron microscopy Aerosol Tungsten alloy

15. NUMBER OF PAGES

88

16. PRICE CODE

17. SECURITY CLASSIFICATION OF REPORT

UNCLASSIFIED

18. SECURITY CLASSIFICATION OF THIS PAGE

UNCLASSIFIED

19. SECURITY CLASSIFICATION OF ABSTRACT

UNCLASSIFIED

20. LIMITATION OF ABSTRACT

SAR

ACKNOWLEDGMENT

The author acknowledges the contributions of Cornelius Wolff, Robin Gibson, Ray Murk, and Gwendolyn McKinney at Aberdeen Proving Ground and Richard Fliszar, Mara Mortman, Fee M. Lee, and Moon Chung at Picatinny Arsenal.

DTIC QUALITY INSPECTED 3

CONTENTS

	Page
Introduction	1
Materials and Methods	1
Projectiles and Targets	1
Video	2
Sample Collection	2
Gravimetric Analysis	3
Scanning Electron Microscopy and X-ray Energy Dispersive Spectrometry	3
X-ray Diffraction	3
Metallurgical Evaluation of Fragments	3
Inductively Coupled Plasma-Atomic Emission Spectrometry	4
Results and Discussion	4
Overview	4
Gravimetric Analysis	4
Scanning Electron Microscopy and X-ray Energy Dispersive Analysis	5
Scanning Electron Microscopy and X-ray Energy Dispersive Analysis of Dust Particles and Larger Fragments	7
X-ray Diffraction Spectrometry	7
Metallurgical Evaluation of Fragments	7
Inductively Coupled Plasma-Atomic Emission Spectrometry	8
Conclusions	8
Recommendations	9
References	61
Appendix A – Tables	63
Distribution List	79

FIGURES

	Page
1 Assemblage of particles on stage 8	13
2 Region of the assemblage shown in figure 1	13
3 Agglomeration of particles on stage 8	13
4 X-ray energy dispersive spectrograph of the elemental composition of a region of the agglomeration shown in figure 3	13
5 Overview of fine particles present on stage 8 from shot 1	15
6 X-ray energy dispersive spectrograph of the elemental composition of the specimen illustrated in figure 5	15
7 Agglomeration of fine particles on stage 8 from shot 1	17
8 X-ray energy dispersive spectrograph of the elemental composition of the specimen illustrated in figure 7	17
9 Agglomeration of particles embedded in impaction compound	19
10 X-ray energy dispersive spectrograph of the elemental composition of the specimen illustrated in figure 9	19
11 Assemblage of fine particles on stage 7	21
12 View of numerous fine particles on stage 7 from shot 1 at high magnification	23
13 X-ray energy dispersive spectrograph of the elemental composition	23
14 Agglomerations (large arrow and arrow head) and individual particles (small arrow) present on stage 7 from shot 1	25
15 X-ray energy dispersive spectrograph of the elemental composition of an agglomeration illustrated in figure 14 (large arrow)	25
16 X-ray energy dispersive spectrograph of the elemental composition of an agglomeration illustrated in figure 14 (arrow head)	25
17 X-ray energy dispersive spectrograph of the elemental composition of a particle illustrated in figure 14 (small arrow)	25

FIGURES (cont)

	Page
18 Overview of the particles collected on stage 1 from shot 4	27
19 Detail of specimens illustrated in figure 18	27
20 Overview of particles collected on stage 2 from shot 4	29
21 Detail of the specimen illustrated in figure 20 (arrow)	29
22 X-ray energy dispersive spectrograph of the element composition of one of the particles shown in figures 20 and 21 (arrow)	29
23 Agglomeration of particles on stage 2 from shot 4	31
24 X-ray energy dispersive spectrograph of the elemental composition of the agglomeration illustrated in figure 23	31
25 Overview of particles embedded in impact compound on stage 3 from shot 4	33
26 X-ray energy dispersive spectrograph of the elemental composition of one of the specimens illustrated in figure 25	33
27 Overview of specimens present on stage 4 from shot 4	35
28 Details of specimens present on stage 4 from shot 4	35
29 X-ray energy dispersive spectrograph of the elemental composition of one of the particles illustrated in figure 28	35
30 Overview of particles on stage 4 from shot 4	37
31 X-ray energy dispersive spectrograph of the elemental composition of one of the particles illustrated in figure 30 (arrow)	37
32 Overview of particles on stage 5 from shot 4	39
33 Details of particles on stage 5 from shot 4	39
34 X-ray energy dispersive spectrograph of the elemental composition of one of the particles illustrated in figure 33 (arrow)	39
35 Overview of particles collected on stage 6 from shot 4	41

FIGURES (cont)

	Page
36 X-ray energy dispersive spectrograph of the elemental composition of one of the particles illustrated in figure 35	41
37 Overview of particles and agglomerations of particles on stage 8 from shot 4 (compare with figure 1)	43
38 Detail of a region illustrated in figure 37 (compare with figure 2)	43
39 X-ray energy dispersive spectrograph of the elemental composition of one of the agglomerations illustrated in figure 38	43
40 Dust particle (with satellites) retrieved from a cyclone collector	45
41 X-ray energy dispersive spectrograph of the elemental composition of the particle illustrated in figure 40	45
42 Fragment from the residue that remained on the test platform after a shot	47
43 Detail of the specimen illustrated in figure 42	47
44 X-ray energy dispersive spectrograph of the elemental composition of the fragment illustrated in figure 42	47
45 Specimen selected from the residue that remained on the test platform after a shot	49
46 Detail of the surface of the specimen shown in figure 45	49
47 X-ray energy dispersive spectrograph of the elemental composition of a region on the specimen illustrated in figures 45 and 46	49
48 Specimen selected from the residue that remained on the test platform after a shot	51
49 X-ray energy dispersive spectrograph of the elemental composition of a region on the specimen illustrated in figure 48	51
50 Specimen selected from the residue that remained on the test platform after a shot	53
51 X-ray energy dispersive spectrograph of the elemental composition of a region on the specimen illustrated in figure 50	53

FIGURES (cont)

	Page
52 Specimen retrieved from a cyclone collector	55
53 X-ray energy dispersive spectrograph of the elemental composition of a region on the specimen illustrated in figure 52	55
54 Fragment selected from the residue that remained on the test platform after a shot	57
55 X-ray energy dispersive spectrograph of the elemental composition of a region on the particle illustrated in figure 54	57
56 Fragment selected from the residue that remained on the test platform after a shot	59
57 X-ray energy dispersive spectrograph of the elemental composition of a region on the fragment illustrated in figure 56	59

INTRODUCTION

A survey of the literature indicates that for tungsten alloys used in kinetic energy (KE) penetrators, priority health and the environmental topics requiring clarification are the possible health risks resulting from exposure to metallic aerosols, environmental transport, and uptake by biota (ref 1). Tungsten itself is generally viewed as benign. The presence of two toxic metals in the alloy, nickel, and cobalt, although in relatively small proportions, raises issues about the possible risks that may be associated with (a) inhalation of aerosols and (b) ingestion of the metals once they are introduced into the food chain.

The principal pathway for entry of metals into the body when a KE penetrator is fired into a hard target is inhalation of the aerosols. Not much is known about the physical and chemical nature of aerosolized particles produced during tests using tungsten alloy penetrators, or about the biological processes involved in removing them from the lungs once they have been inhaled. Only one analysis has been performed to date that deals with the solubility of tungsten alloy aerosols in lung fluid (ref 2).

Considerable attention has been directed toward the effects of cemented tungsten carbide (hardmetal) dust on industrial workers' health (ref 3). Extrapolation of the health findings on hardmetal disease to individuals exposed to aerosols from KE penetrators is risky. First, the metals used in penetrator alloys are different from those ordinarily found in hardmetal; second, the temperature at the time the aerosols are produced could have a significant effect on the oxides produced, hence on particle solubility. Temperature effects in relation to particle solubility have been demonstrated for various metals (ref 4). Experimental work led one investigator to suggest that temperature conditions during formation of a complex mixture of oxides (predominantly uranium dioxide) may have been more important as a determinant of solubility than particle size (ref 5).

In this study, the physical and chemical characteristics of shape, size, and elemental composition of aerosols and dust particles were analyzed using a scanning electron microscope equipped with an x-ray energy dispersive spectrometer (EDS). Additional tests were also performed including metallurgical, chemical, and x-ray powder diffraction.

MATERIALS AND METHODS

Projectiles and Targets

The ammunition used in these tests was armor-piercing fin stabilized discarding sabot with tracer (APFSDS-T) 120-mm cartridges. The KE penetrator subassemblies made of tungsten (92.85 %), nickel (6 %), iron (1 %), cobalt (0.15 %), and traces of manganese were equipped with a steel tip, aluminum alloy windshield, and tail fin assemblies. The elements present in these two aluminum alloy assemblies include magnesium, silicon, copper, chromium, and zinc.

The targets were rolled homogeneous armor (RHA) plates made of an iron-carbon alloy with other elements added as modifiers. The other metals used in manufacturing the RHA include the following: chromium, manganese, molybdenum, nickel, vanadium, phosphorus, and silicon. Typically, the steel has approximately 1% each of chromium and manganese; the other elements are generally present in concentrations less than 1%. Overall target thickness was sufficient to ensure that the penetrator would not completely perforate the target, but would penetrate deeply.

Video

The tests were recorded on videotape to document the size of the dust and aerosol cloud generated by the penetrator impact under different test conditions.

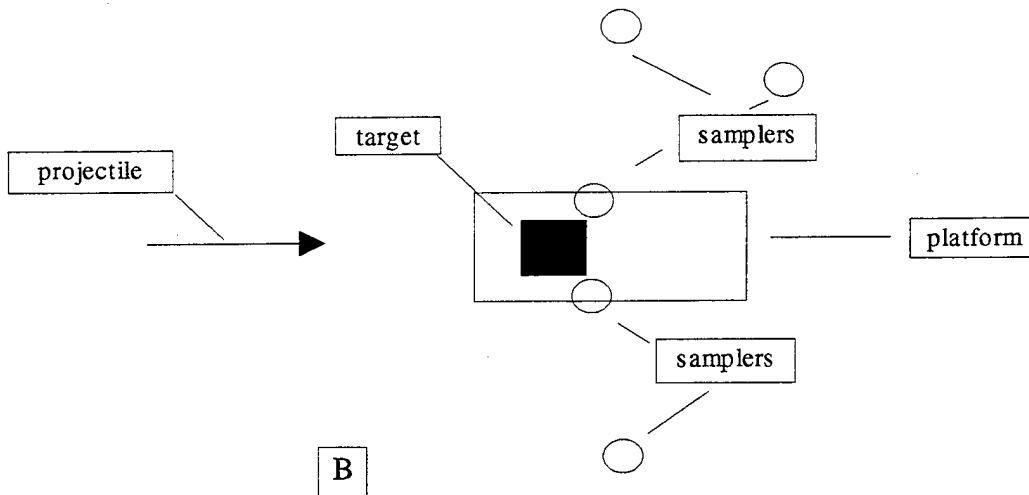
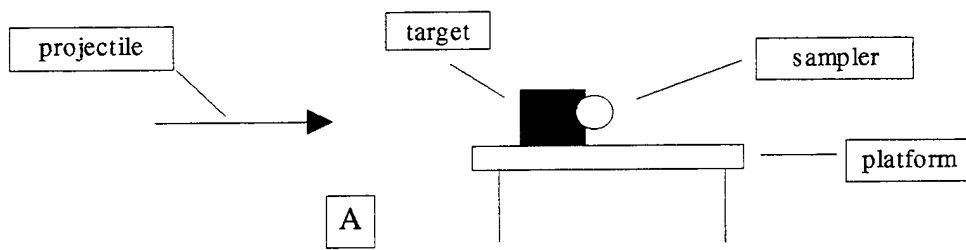
Sample Collection

Eight-stage Sierra Marple Personal Cascade Impactors (model 298) were used to collect the aerosol samples (ref 6). The cut points of the stages range from 21 to 0.35 μ . The substrates were made of Mylar and were coated with impaction compound (Dow-Corning Silicon Release Spray) to improve retention of the sample. After the release spray was applied, substrates were placed inside a desiccator and dried for at least 48 hrs before being inserted into an impactor. The airflow through each unit was calibrated at the test site (A.P. Buck, model M-30).

Samples were collected in the afternoon on 15 through 17 April (shots 1, 2, 3, and 6) and in the morning on 17 April 1996 (shots 4 and 5). Atmospheric temperature at the time of the tests was in the range 46°F to 55°F; relative humidity was in the range 30 to 55%. Wind speed recorded at the Aberdeen Proving Ground Meteorological Center was variable (app A, table A-1).

The placement of the impactors was guided by observations on wind direction made at the test site. A hand-held anemometer (Ames Corp., model RVM 96A) was used as close to firing time as possible—wind direction and speed varied appreciably near the target. Initially, cascade impactors were placed close to the target (approximately 3 ft) to ensure that some of the aerosol would be collected. The impactors were moved to positions 15 ft (side) and 18 ft (side-rear) away from the target for shot 3 to avoid damage from target and penetrator debris. They were left in these positions in subsequent tests. The following diagrams (not drawn to scale) show the positions of the cascade impactors in relation to the target (side view [A] and top view [B]).

The impactors were connected with plastic tubing to a vacuum pump and manifold assembly positioned and shielded for protection beneath the platform supporting the target. The tubing leading to the impactors was also shielded for protection against stray fragments. An operator located in a remote protected shelter when the shot was fired switched on the vacuum pump; the pump was turned off about 5 min later.



Gravimetric Analysis

The amount of material collected on the coated Mylar substrates was determined by standard weighing techniques using a Mettler AE240 balance.

Scanning Electron Microscopy and X-ray Energy Dispersive Spectrometry

These analyses were accomplished using an Amray scanning electron microscope (Model 1830 Turbo) equipped with a Princeton Gamma Tech (PGT System 4 Plus) x-ray EDS. Specimens were coated with gold-palladium alloy in a Denton sputter coater before examination and x-ray analysis. Coating was done to enhance sample conductivity and to avoid electron-beam damage to the Mylar substrate.

X-ray Diffraction

Fragments collected from the platform after a test were pulverized by hand using a mortar and pestle, and then analyzed in a Siemens Diffractometer (Model D500) and in a Siemens Spectrum Analyzer (Model SRS 303). Information was obtained for selected oxides that were present in the dust and fragment residue.

Metallurgical Evaluation of Fragments

Particles ejected from the penetration tunnel were collected from the target platform and evaluated for metallurgical characteristics under a light microscope. Sample preparation included embedding in epoxy, grinding and polishing the sample with silicone carbide paper and diamond paste, and etching the specimen chemically.

Inductively Coupled Plasma-Atomic Emission Spectrometry

The amount of material collected in the cascade impactors was small, so the substrates were pooled before the chemical analyses were performed, i.e., stages 1 to 3; stages 4 and 5; stages 6 and 7; and stage 8. The cellulose ester filter positioned at the end of the impactor substrate train was treated separately. Each of the samples (five per impactor) was then dissolved in a solution of hot acid (1:4 perchloric acid: nitric acid) and heated. Finally, the residue was taken up in a portion of the acid solution and brought to volume with distilled water. The detection limit for the EPA method used (7300) was 0.05 mg/L for each of the metals analyzed, i.e., cobalt, nickel, iron, and tungsten.

RESULTS AND DISCUSSION

Overview

The videotape shows the formation of a dust and aerosol cloud at impact and then its rapid dispersal due to gusty winds. There were no visible signs of the cloud in the area when personnel returned to inspect the target 2 to 5 min after the shot was fired. The fragments and dust particles settled to the ground rapidly due to their high densities. Follow-up studies designed to provide information about atmospheric transport and fallout of particles in the aerosol fraction are in progress (ref 7).

Gravimetric Analysis

During the first two shots, the rates of air flow through the impactors—approximately 4 liters per minute (LPM)—were outside the manufacturer's recommended range, but less than the manufacturer's suggested upper limit of 5 LPM. Accordingly, the cut sizes of the impactor stages were recalculated, taking the 4-LPM flow rate into consideration. In subsequent tests, the flow rates were adjusted to 1 to 3 LPM (nominally 2 LPM).

The mass of material deposited on the Mylar substrates was obviously low (app A, tables A-2 to A-19). A hand lens or microscope was needed to see the accumulations of particles trapped on most of the substrates. Because the reproducibility of the measurements was 0.02 mg (standard deviation using a Mettler AE240 balance), many of the values reported in the tables should be viewed as too low to be measured with accuracy.

The fact that only a small amount of material was collected during these tests is attributed to two factors. First, the tests were conducted in the open air; this produced an enormous dilution effect. Second, the thickness of the targets may have limited the amount of aerosol exiting the penetration tunnel. Gusty winds on the test day contributed considerably to the dilution effect.

Scanning Electron Microscopy and X-ray Energy Dispersive Analysis

There is overlap in the peaks attributable to the K_{α} for silicon (1.739 Kev) and to emissions from the tungsten M shell (1.774 Kev). However, it is possible to differentiate between the two elements by considering the emissions from the L shell of tungsten as well. Where these characteristic peaks were present, the prominent peak near 2.0 Kev was attributed to tungsten; where they were absent, the peak near 2.0 Kev was attributed to silicon. The possible sources of silicon in the samples are the impaction compound, the aluminum alloys used in the windshield and tail fin assemblies, and the target material.

Figure 1 shows one of the 12 assemblages of aerosol particles that were collected on substrate 8 during shot 1. Although the distribution of sizes appears at first glance to be inconsistent with the cut point of the stage (which for this sample was 0.35μ), at high magnification the structures can be seen to be agglomerations of fine particles (figs. 2 and 3). Details of one of the unusual agglomerations present in the photographic field is shown in figure 3 and the EDS spectrum for the mass is shown in figure 4. Examination of particles separated from a substrate is planned so the individual components of the agglomerates can be displayed.

Nondescript spherical particles were found on all of the substrates examined. They were common at the edges of the impacted zones on the Mylars, i.e., at the edges of the accumulations found directly below the slots or circles machined into the impactor supports. An example of the fine spherical specimens present on substrate 8—approximately 0.2μ in diameter—is shown in figure 5; the EDS spectrum obtained at high magnification for this specimen revealed that it was made of tungsten and nickel (fig. 6).

One explanation that accounts for the rounded shapes that were found in the aerosol fraction is that the particles were formed when metals were ejected from a penetration tunnel, burned in air, and cooled. Other possibilities, however, are: (1) they originate as splash from molten metal produced during penetration and (2) they are generated by vaporization of metals followed by condensation. References 8 and 9 discuss mechanisms of penetration and melting—of matrix elements and target materials—as a result of high temperatures generated during tunneling. Magness (ref 8) cited a melting temperature of approximately 1500°C for a nickel-based alloy. Gerlach (ref 9) commented that, for a tungsten penetrator in contact with the iron in target steel, the melting point is lowered from 3400°C to 1650°C . Gerlach concluded from one test involving a tungsten penetrator that the specimen he examined had been quenched from temperatures greater than 1300°C .

The presence of aluminum in many of the EDS spectra presented in this report suggests that a portion of the aluminum alloy associated with the windshield and tail fin

assemblies may have been vaporized and plated onto some of the tungsten-containing particles. Additional information is needed regarding the possibility that penetrator alloy matrix may also be vaporized at impact and during tunneling. Tungsten oxide is known to vaporize in the range 1200° to 1300°C (refs 10 through 12).

Figures 7 to 10 show large agglomerates on stage 8 during shot 1 and their EDS spectra. The surface structure of an angular specimen shown in figure 9 was lost due to its immersion in the impaction compound. Figure 11 illustrates one of 12 assemblages of particles collected on the stage 7 Mylar during shot 1 where the cut size of the particles was 0.64 μ . Additional specimens collected during shot 1 and their EDS spectra are illustrated in figures 12 to 17.

Assemblages of particles from sequential substrates in a single impactor and the EDS spectra of selected particles are shown in figures 18 to 39. Reasonably good separation according to particle size is apparent on these substrates (figs. 27 and 30). This is presumed to be a result of differences in the abundance of material collected (i.e., there was less chance of agglomeration) and in the density of the particles within a given size range (particles of similar size, shape, and density have similar aerodynamic diameter equivalents).

Samples were collected approximately 3 ft from the target during shot 1 and approximately 18 ft away during shot 4. (The cascade impactors were moved after the first two shots because debris generated at impact was seen as potentially damaging to samplers placed within a radius of a few feet of the impact.) A comparison of figures 1 and 37 shows greater mass accumulated on the stage 8, shot 1 Mylar substrate (cut size dimension 0.35 μ) than on the stage 8, shot 4 Mylar substrate (cut size dimension 0.5 μ). It is recognized, however, that fallout between 3 and 18 ft may not be the only factor that affected the mass that was accumulated and that numerous other explanations for the differences are possible. Other explanations to account for the differences in mass include asymmetric dispersion of particles from the penetration tunnel as target material was eroded and the effects of wind on the fine airborne particles.

Variation was observed in the elemental composition of particles from impactors placed in different locations. Tungsten, for example, was frequently found as a component of the particles collected during shot 1—where the impactor had been placed close to the target. Tungsten was found less often in specimens collected during shot 4 where the aerosol appeared to be made up predominantly of target material.

The elemental composition of the particles analyzed varied appreciably from one specimen to another. When tungsten was detected in a specimen, it was usually associated with the presence of iron and nickel, both of which are present in the target and in the penetrator matrix.

Cobalt was detected in the dust and fragment fraction by means of x-ray powder diffraction analysis. Cobalt was found only as traces that were not immediately evident in the

EDS analysis. The fact that only trace amounts were detected is attributed to its initial low concentration in the tungsten alloy, to the small sizes of the specimens examined, and to the fact that the cobalt peak is partially obscured by iron.

Scanning Electron Microscopy and X-ray Energy Dispersive Analysis of Dust Particles and Larger Fragments

Figure 40 shows a specimen deposited in a cyclone collector; a EDS analysis is given in figure 41.

The residue left behind on the target platform could not be identified by eye as penetrator material. Some bright metallic fragments suspected of containing aluminum were found. The EDS analysis of one of the specimens revealed a strong aluminum peak (figs. 42 to 44) as well as the presence of other elements present in the two alloys used to fabricate the tail fin and windshield, i.e., magnesium, copper, chromium, and zinc.

Specimens were selected from the dust and fragment fraction in an effort to match shapes or structure with elemental content of the specimen. No pattern was found that could be used to predict the composition of a sample. Examples of the dust particles and their elemental compositions are shown in figures 45 to 53.

The fragment shown in figure 54 is free of tungsten and is, therefore, assumed to originate with the target (see the spectrum in figure 55). The specimen shown in figure 56, on the other hand, clearly originated with the penetrator (fig. 57).

X-ray Diffraction Spectrometry

The elements detected in the dust and fragment sample by means of a x-ray diffraction spectrometer were characteristic of the penetrator and target materials. A computer library of atomic absorption spectra was surveyed to determine whether any of the oxides of tungsten stored in the files was detectable in the sample; none of them was present. However, various metal oxides were identified in the sample: two species of iron oxide (Fe_3O_4 and Fe_2O_3), manganese oxide (Mn_3O_4), and chromium oxide (CrO).

Metallurgical Evaluation of Fragments

Deformation of tungsten grains was observed in fragments of the penetrator selected from the residue remaining on the test pad. Magness and Gerlach (refs 8 and 9) both discussed aspects of the melting process that occurred during penetration. Although the specimen ejected from the mouth of the penetration tunnel during these tests did not provide definitive information about melting, subsequent follow-on studies of fragments deposited far inside a penetration tunnel did show such evidence (ref 13).

Inductively Coupled Plasma-Atomic Emission Spectrometry

Samples were consolidated prior to chemical analysis. Because of this, the concentrations reported in tables A-20 to A-22 cannot be related to a single size fraction. Particularly noteworthy in this analysis, however, is the fact that cobalt was below the level of detection of the analytical procedure (0.05 mg/L) in all of the samples examined.

The concentration of nickel exceeded the level of detection in only three instances (app A, table A-20).

Only four concentrations of tungsten were greater than the level of detection and they are given in appendix A, table A-21. The analytical procedure that was used may not have completely solubilized the tungsten-containing particles. No conclusion can be drawn, therefore, regarding the concentration of tungsten present on the impactor stages. Improvements in chemical digestion are being investigated to ensure that in future testing, tungsten-containing particles are completely dissolved.

Detectable levels of iron were found in more than 50% of the samples examined; the concentrations (in mg/m³) are summarized in appendix A, table A-22. The concentrations of iron were generally highest on the consolidated substrates from impactor stages 1 through 3. The concentrations for these upper stages of the impactors ranged from a low value of 0.19 mg/m³ on stages 1 to 3 for shot 3-W1044 to a high value of 10.26 mg/m³ for comparable stages from shot 2.

CONCLUSIONS

1. The mass deposited on the Mylar substrates was low. Most of the samples collected were too small to be seen with the unaided eye. (Samples were too small to be measured with accuracy using the balance that was available for this study.) Dilution in air and possibly the thickness of the armor target used in these tests are suspected to account for the small samples collected in the impactors.
2. Individual particles as small as 0.2 μ were observed under the scanning electron microscope. (Particles tended to form agglomerations on the Mylar substrates and this gave the appearance of there being large specimens present. Methods are being developed to separate the agglomerated particles from the substrate to allow direct measurements to be made of the number of particles present.)
3. The aerosolized material consisted mostly of small spherical bodies. Three explanations are proposed to account for their shapes: burning in air, splash, and possibly, vaporization followed by condensation.
4. Under the scanning electron microscope, the amount of material collected appeared to depend on the position of the impactor in relation to the target. As expected, the samplers closest to the target provided the most material. The concentrations of

aerosols found in these tests cannot be extrapolated to concentrations produced in an enclosed space (such as inside a tank).

5. Variations were observed in the elemental composition of particles present in different cascade impactors. The station-to-station differences are attributed to the position of the impactor in relation to the target and to the direction and strength of the wind throughout the collection period.
6. Tungsten was usually found in aerosols in association with aluminum and with the metals used to manufacture the penetrator and the target.
7. For the analyses using wet chemistry, the sample size was too small to provide definitive information on the metals present in the aerosol.
8. The failure to detect cobalt in the aerosol using the inductively coupled plasma technique is noteworthy. This is attributed to its initial low concentration in the tungsten alloy and to the small sample that was available for the study. However, cobalt was detected in the dust and fragment fraction and in some of the x-ray spectra.
9. The shapes of the particles present in the dust sample cannot be used to predict their elemental composition.
10. The tungsten oxides present in the dust and fragment residues have not yet been identified by x-ray powder diffraction techniques. Other analytical procedures that can be used to identify the oxides in small specimens are being investigated.
11. Melting is assumed to have occurred in the rolled homogeneous armor (RHA) target and penetrator matrix during these tests.

RECOMMENDATIONS

In future work, it will be important to do the following to expand the database on tungsten alloy aerosols:

- Determine the rate of fall-out of aerosol particles immediately after a shot (in progress).
- Determine the amount of aerosol remaining suspended in the atmosphere in the vicinity of the test pad after a shot. An interval approximating the time spent by workers in the area is recommended (i.e., from 15 to 30 min). (Research on aspects of this recommendation is in progress.)
- Determine the nature of the tungsten oxides present in aerosol samples. A larger sample will be needed than was available for this study. Collection

inside an enclosed target is one way to obtain the quantity of material needed.

- Collect aerosols inside hard targets (armored vehicles) impacted by tungsten alloy penetrators and compare the yield of aerosolized material inside and outside the target.
- Separate the aerosol samples from the Mylar substrates and remove the impaction compound prior to examining the individual particles present in the agglomerations.
- Explore the possibility of using metal from the dust and fragment fraction of the penetrator to produce simulants for use in future solubility studies in lung fluid.
- Determine the effects of temperature on the production of different oxides when particles are formed, and determine the solubility of those particles in lung fluid and in ground water.
- Use a larger sample size than was available for this study, and perform a quantitative analysis of material collected on individual substrates.

Figure 1 Assemblage of particles present on state 8

(This was one of 12 similar assemblages on the Mylar substrate.) Note: The cut size of the particles in this stage is 0.35μ ; the large specimens visible in the photomicrograph are agglomerations of these small particles.

Figure 2 Region of the assemblage shown in figure 1

Numerous fine particles are seen as individual particles in the background. The arrow points to the specimen illustrated in figure 3.

Figure 3 Agglomeration of particles on stage 8

Figure 4 X-ray energy dispersive spectrograph of the elemental composition of a region of the agglomeration shown in figure 3

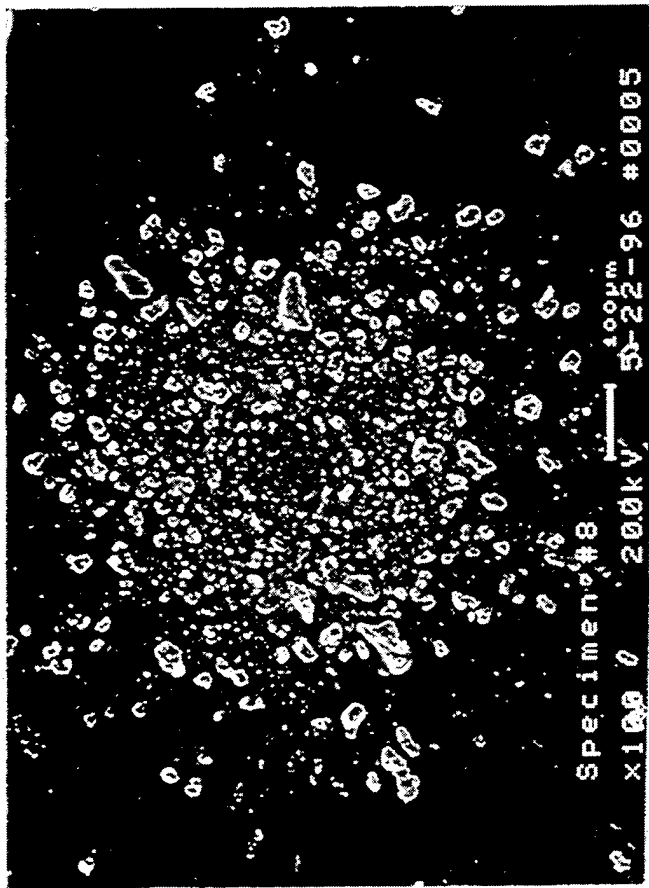


Figure 1

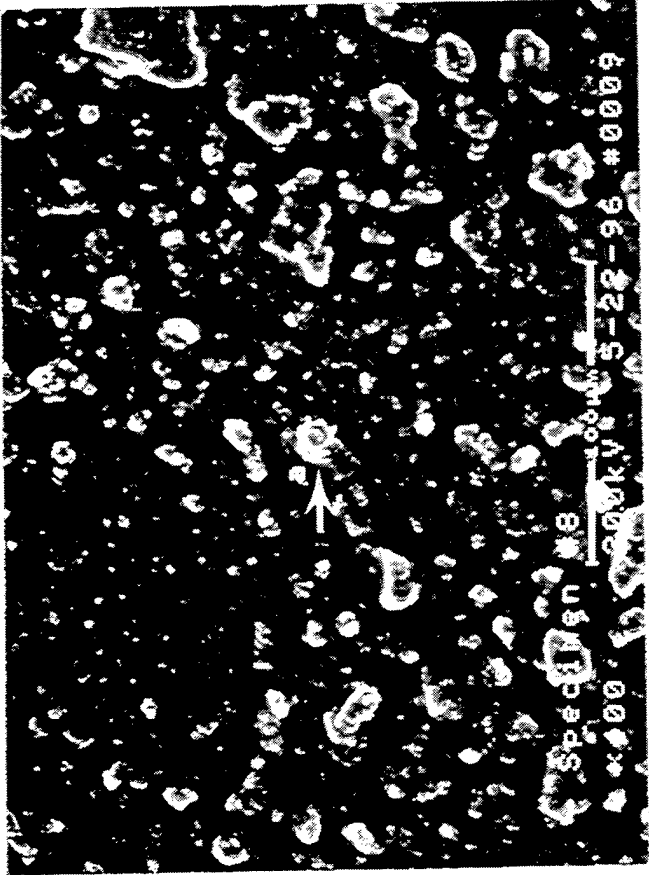


Figure 2

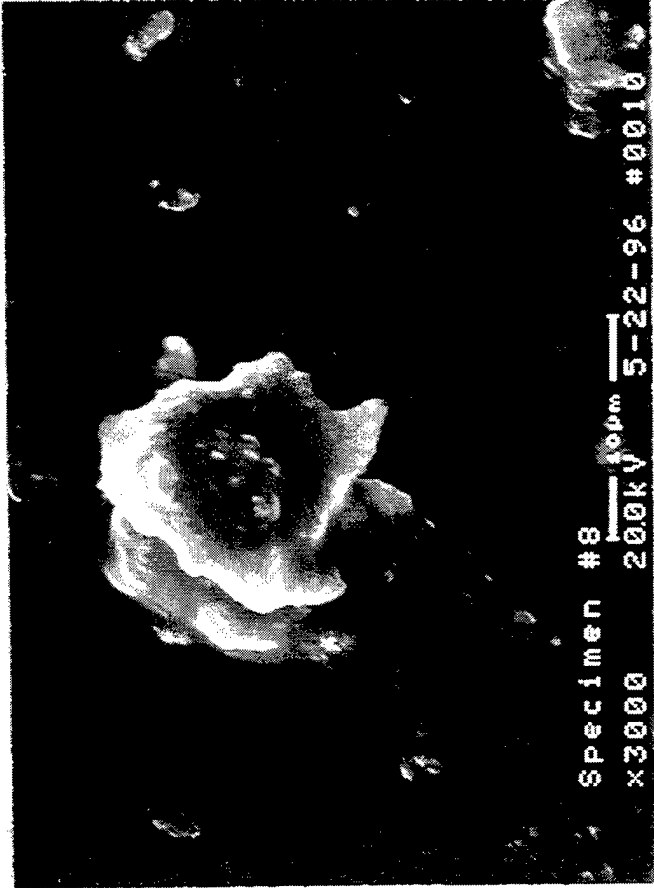


Figure 3

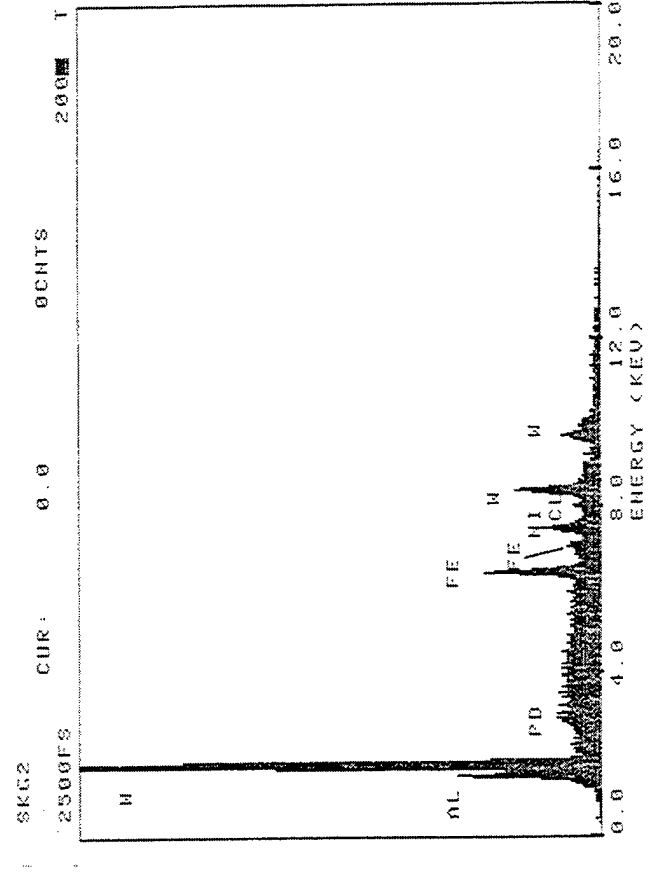


Figure 4

Figure 5 Overview of fine particles present on stage 8 from shot 1

Specimens ranged upward in size from approximately 0.2 μ in diameter (arrow).

Figure 6 X-ray energy dispersive spectrograph of the elemental composition of the specimen illustrated in figure 5

(The EDS analysis was performed at a magnification greater than 4,000 X.)

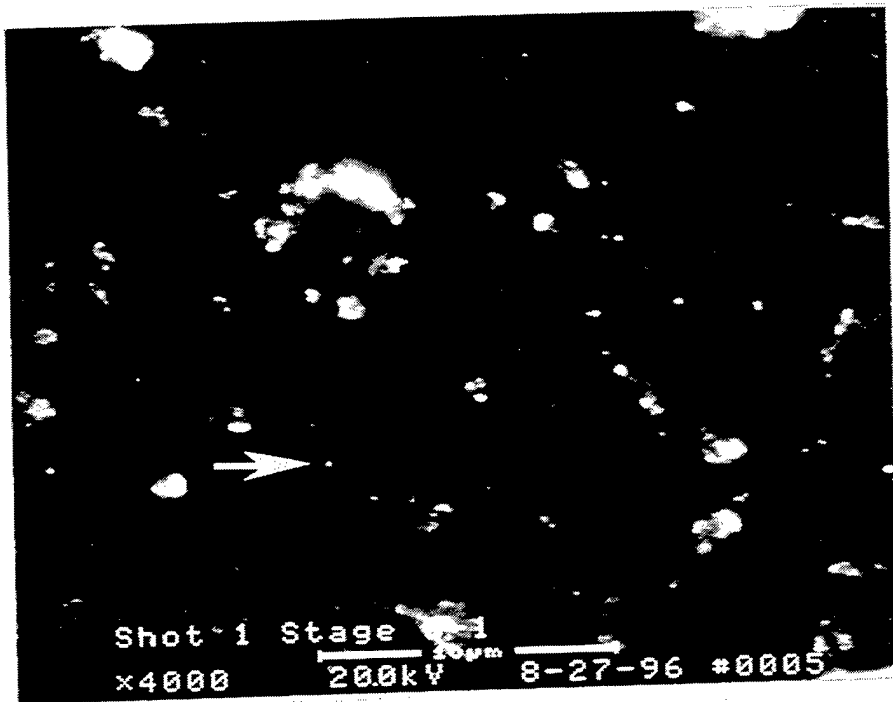


Figure 5

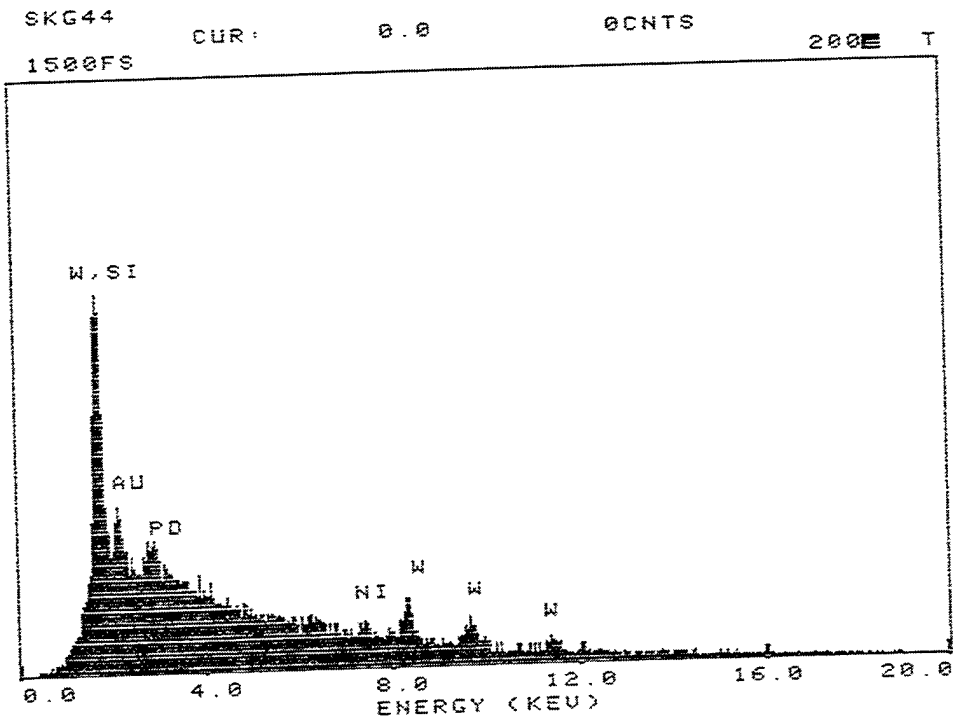


Figure 6

Figure 7 Agglomeration of fine particles on stage 8 from shot 1

Figure 8 X-ray energy dispersive spectrograph of the elemental composition of the specimen illustrated in figure 7



Figure 7

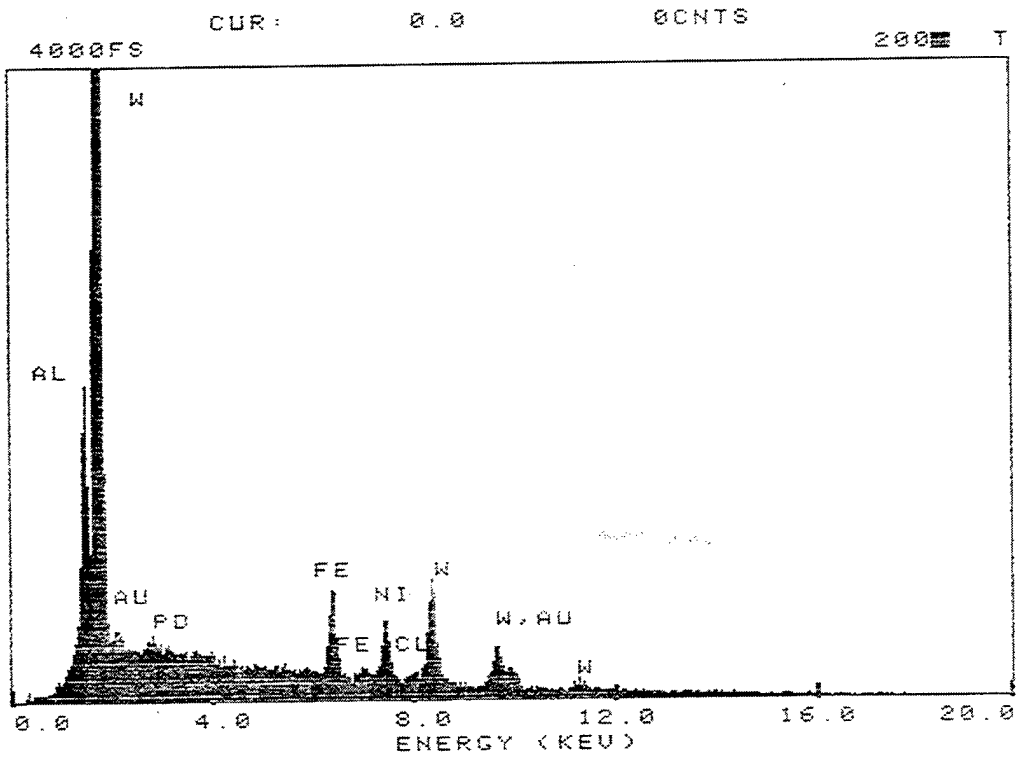


Figure 8

Figure 9 Agglomeration of particles embedded in impaction compound

The arrow indicates the aimpoint of the electron beam when performing the EDS analysis illustrated in figure 10.

Figure 10 X-ray energy dispersive spectrograph of the elemental composition of the specimen illustrated in figure 9

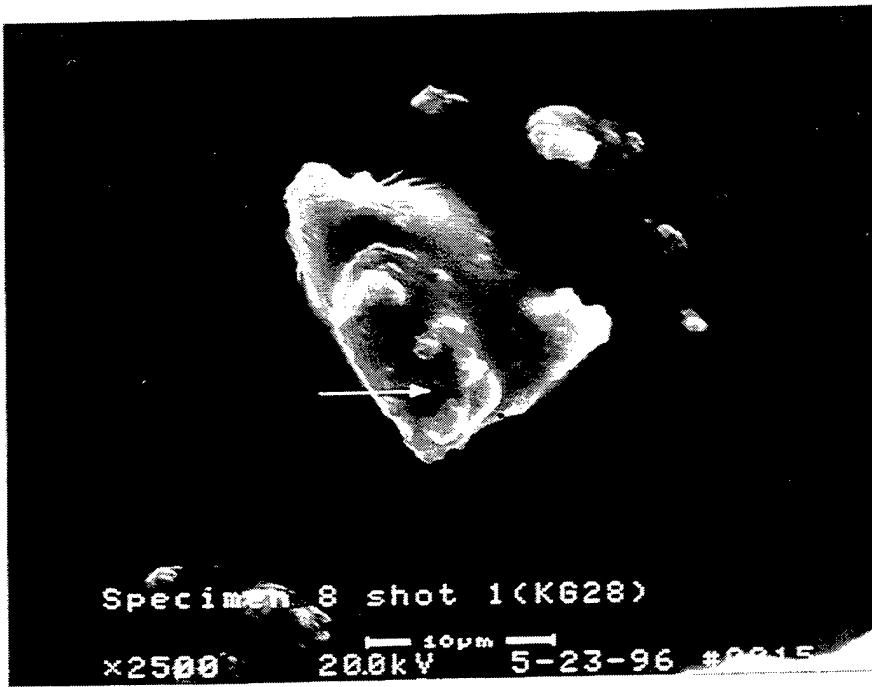


Figure 9

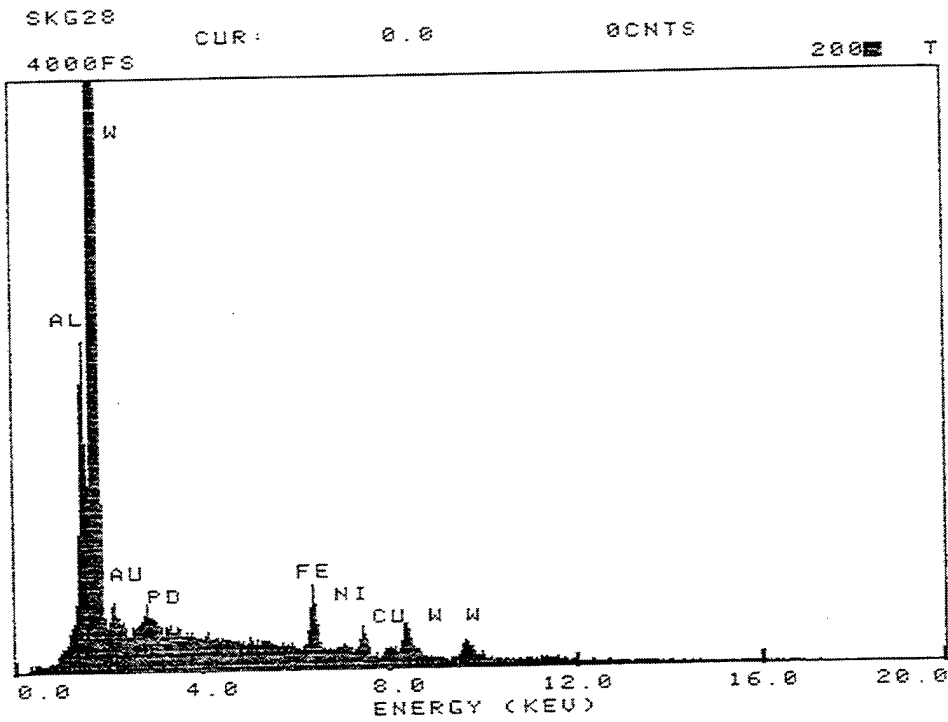


Figure 10

Figure 11 Assemblage of fine particles on stage 7

(This was one of 12 similar assemblages on the Mylar substrate.) Note: The cut size of the particles in this stage is 0.64μ . Note the presence of numerous fine particles and agglomerations.

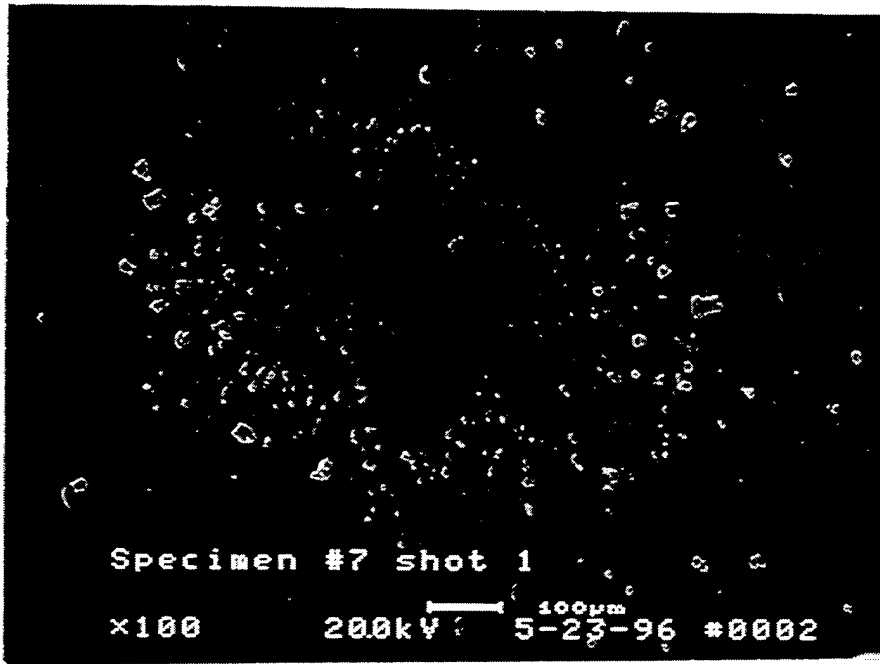


Figure 11

Figure 12 View of numerous fine particles on stage 7 from shot 1 at high magnification

Figure 13 X-ray energy dispersive spectrograph of the elemental composition of the specimen illustrated in figure 12 (arrow)
X-ray data was collected at high magnification.

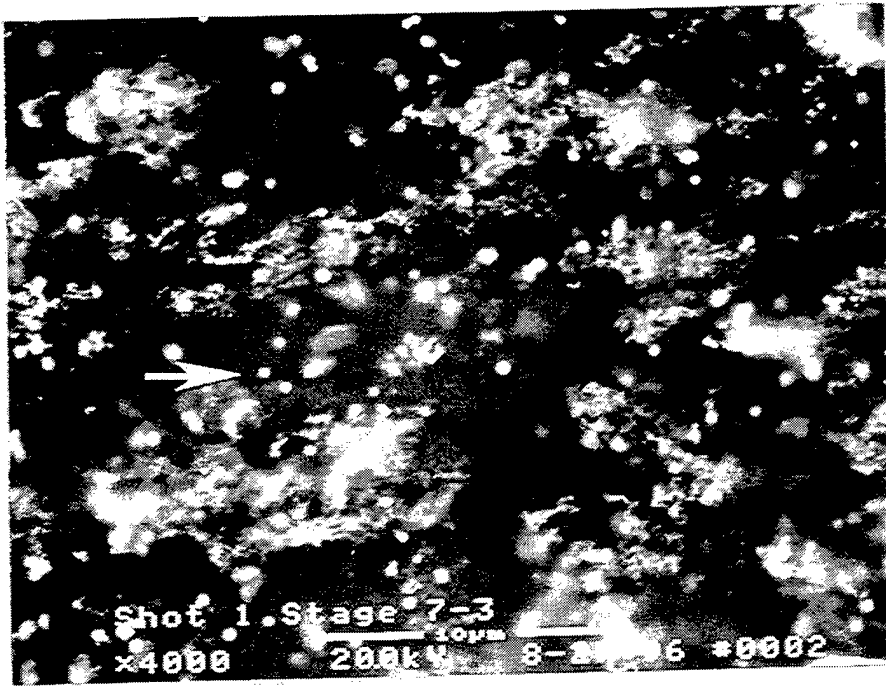


Figure 12

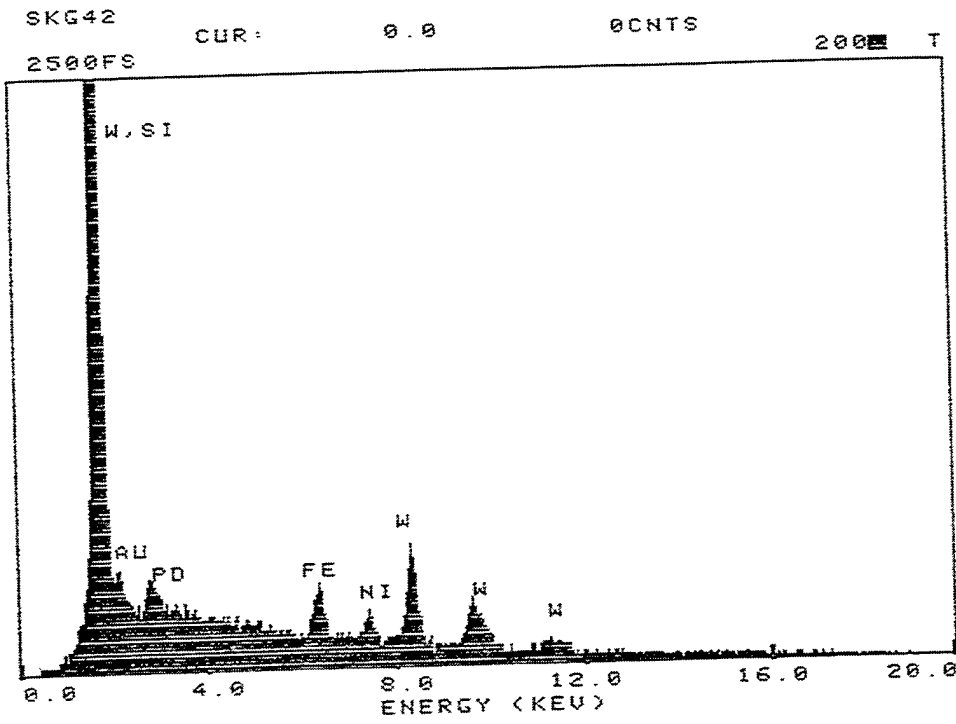


Figure 13

Figure 14 Agglomerations (large arrow and arrow head) and individual particles (small arrow) present on stage 7 from shot 1

Figure 15 X-ray energy dispersive spectrograph of the elemental composition of an agglomeration illustrated in figure 14 (large arrow)

Figure 16 X-ray energy dispersive spectrograph of the elemental composition of an agglomeration illustrated in figure 14 (arrow head)

Figure 17 X-ray energy dispersive spectrograph of the elemental composition of a particle illustrated in figure 14 (small arrow)

Note: X-ray data was collected at high magnification.

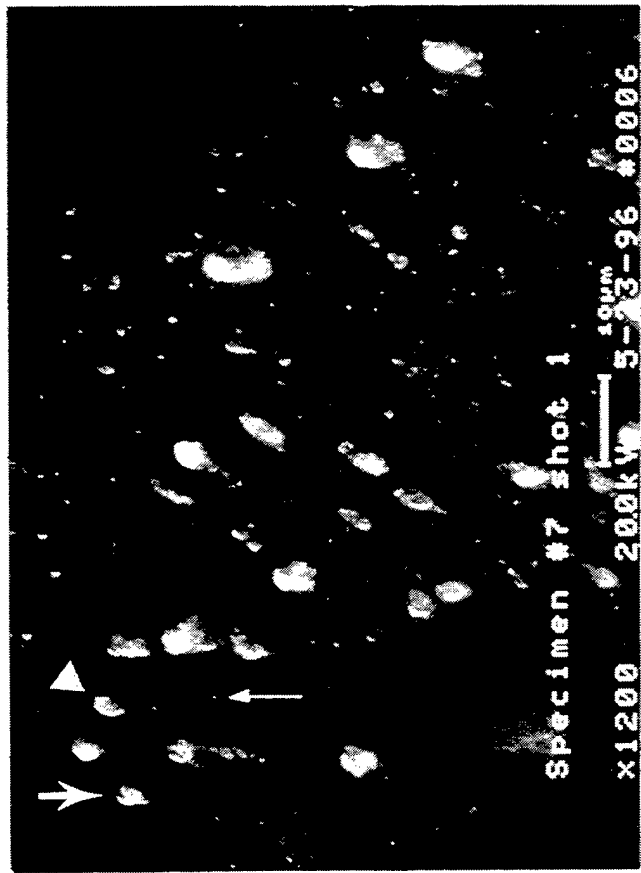


Figure 14

25

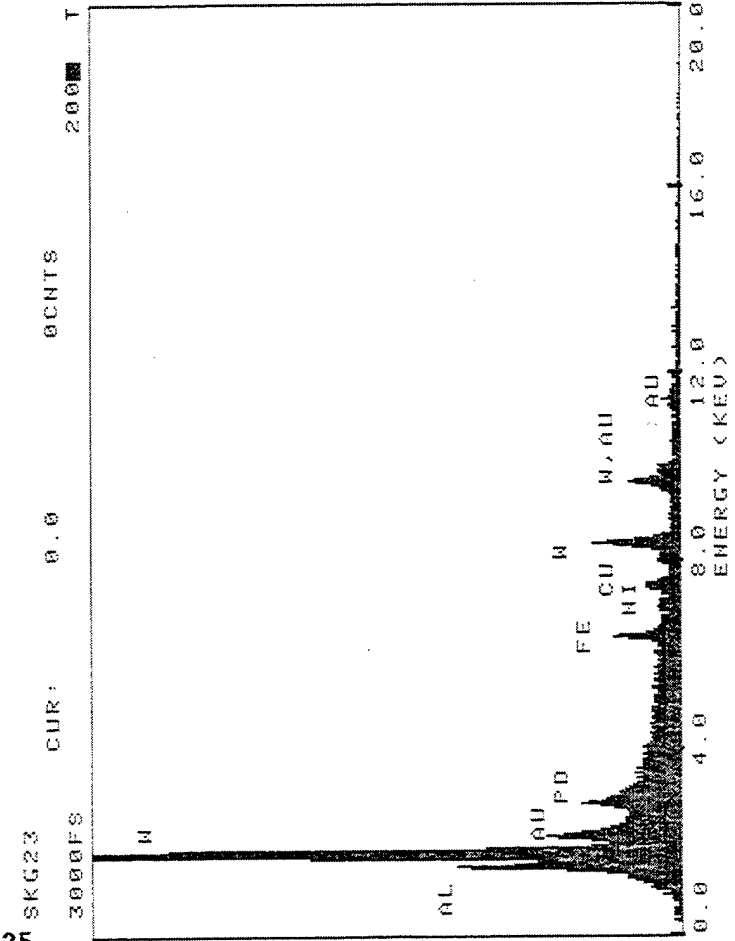


Figure 16

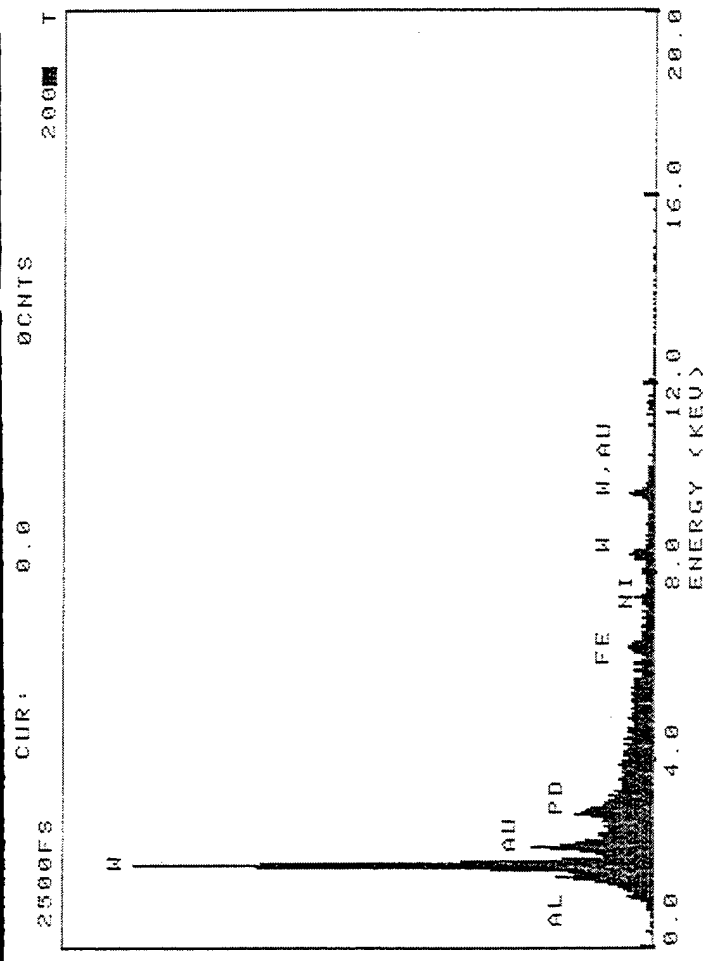


Figure 15

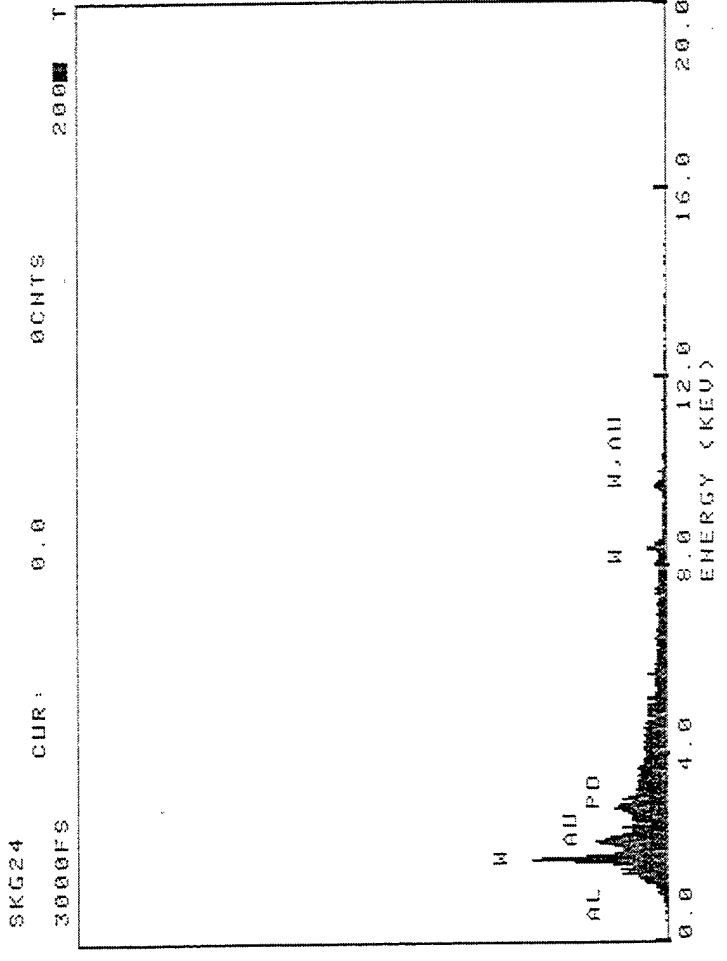


Figure 17

Figure 18 Overview of the particles collected on stage 1 from shot 4

Figure 19 Detail of specimens illustrated in figure 18



Figure 18

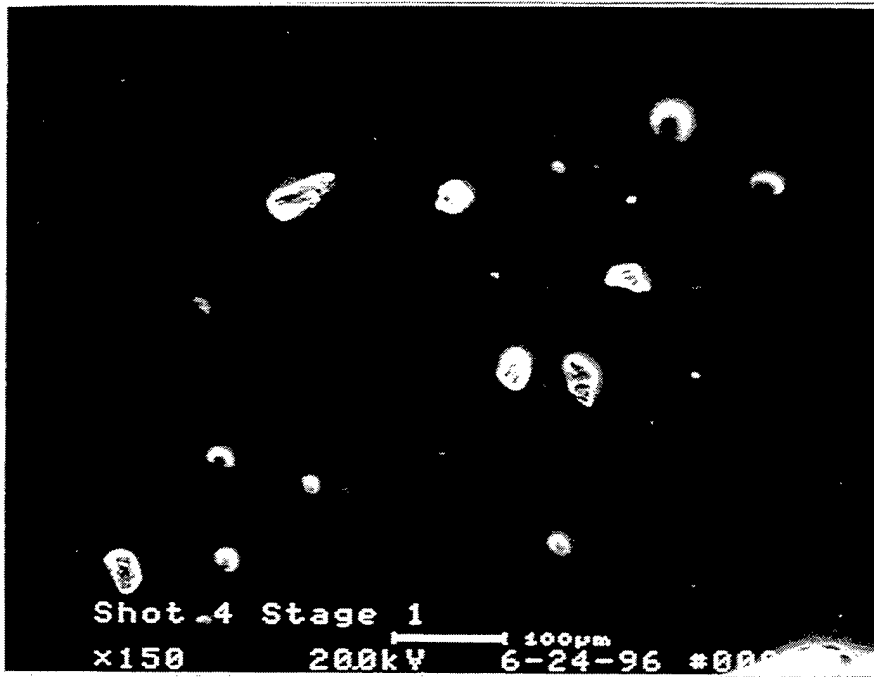


Figure 19

Figure 20 Overview of particles collected on stage 2 from shot 4

Figure 21 Detail of the specimen illustrated in figure 20 (arrow)

Figure 22 X-ray energy dispersive spectrograph of the elemental composition of one of the particles shown in figures 20 and 21 (arrow)

Note the presence of a peak attributable to aluminum and another to the presence of zinc in the spectrum.



Figure 20

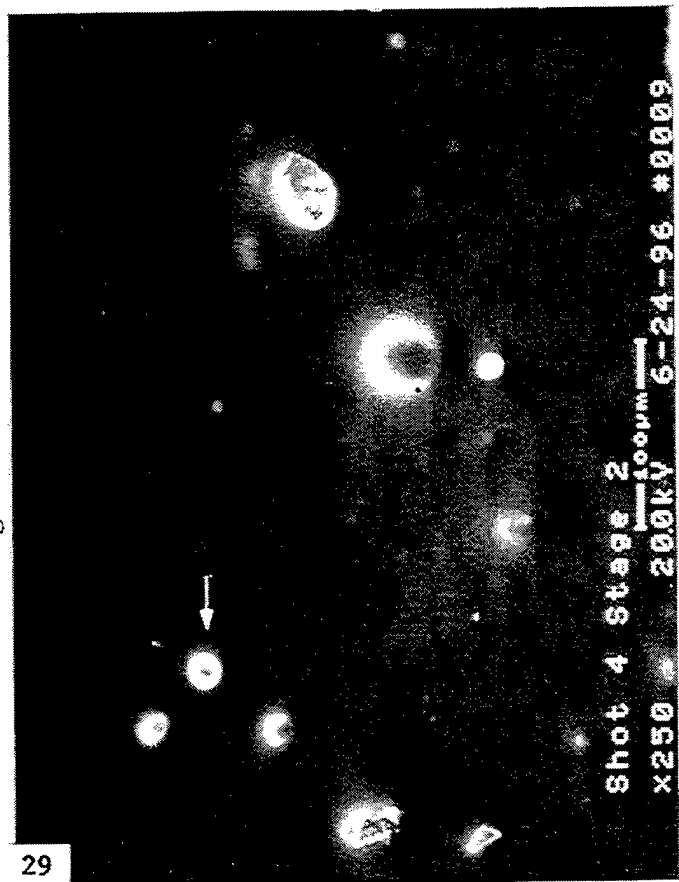


Figure 21

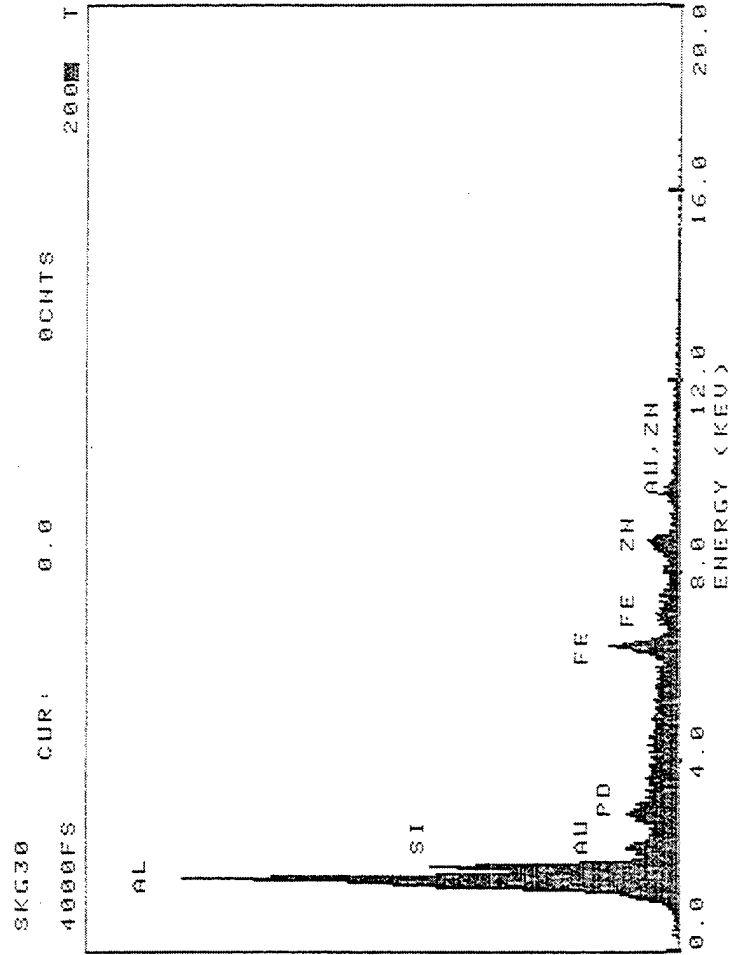


Figure 22

Figure 23 Agglomeration of particles on stage 2 from shot 4

Figure 24 X-ray energy dispersive spectrograph of the elemental composition of the agglomeration illustrated in figure 23

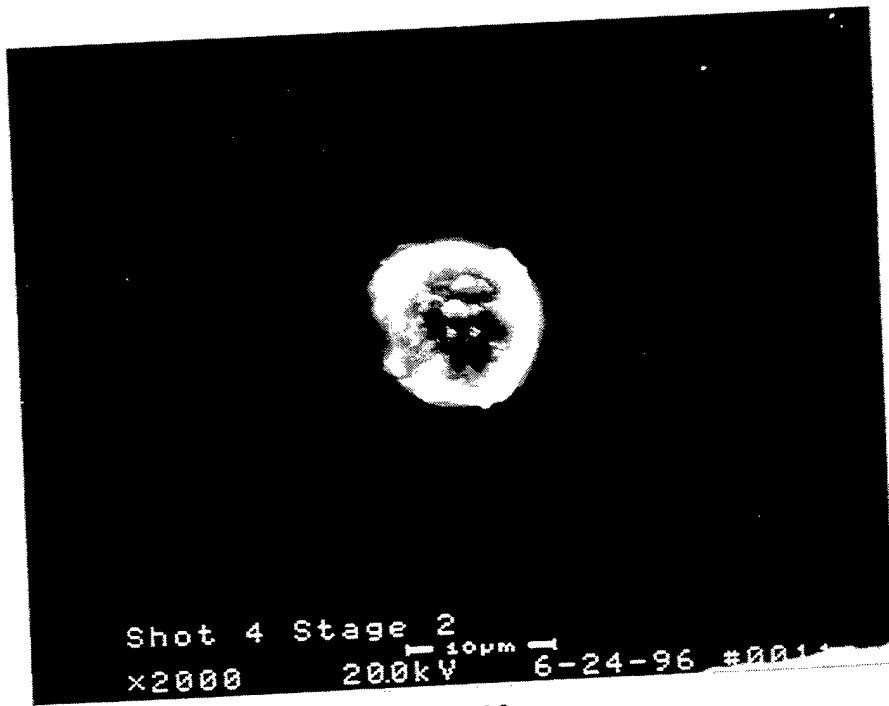


Figure 23

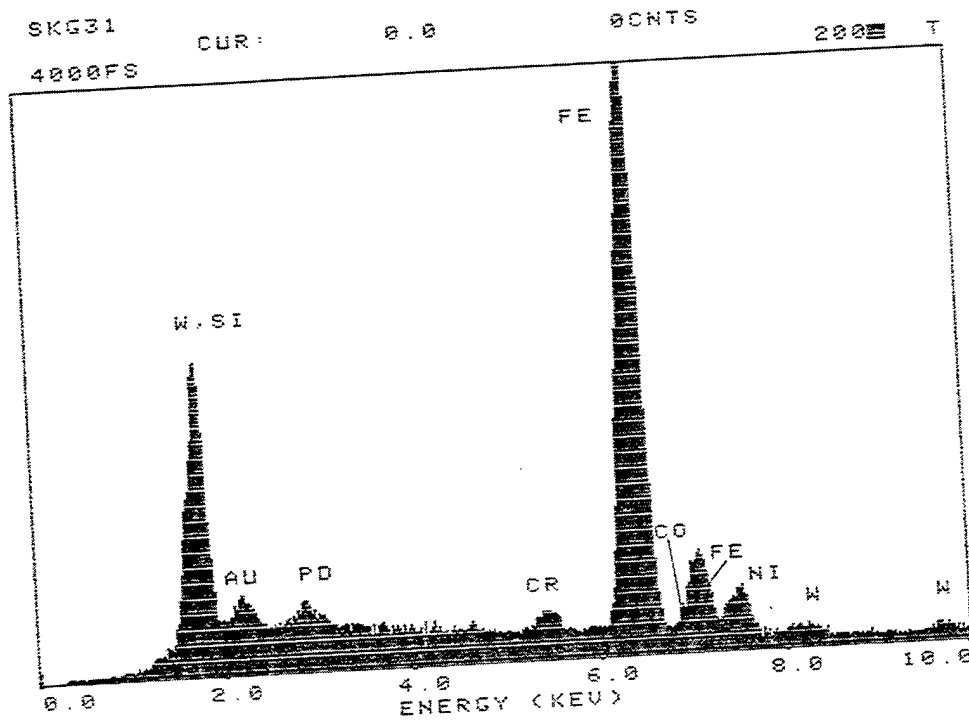


Figure 24

Figure 25 Overview of particles embedded in impaction compound on stage 3 from shot 4

Figure 26 X-ray energy dispersive spectrograph of the elemental composition of one of the specimens illustrated in figure 25

Note the strong silicon peak (impaction compound (?), the presence of aluminum, and the absence of tungsten and matrix metals in the spectrum.



Figure 25

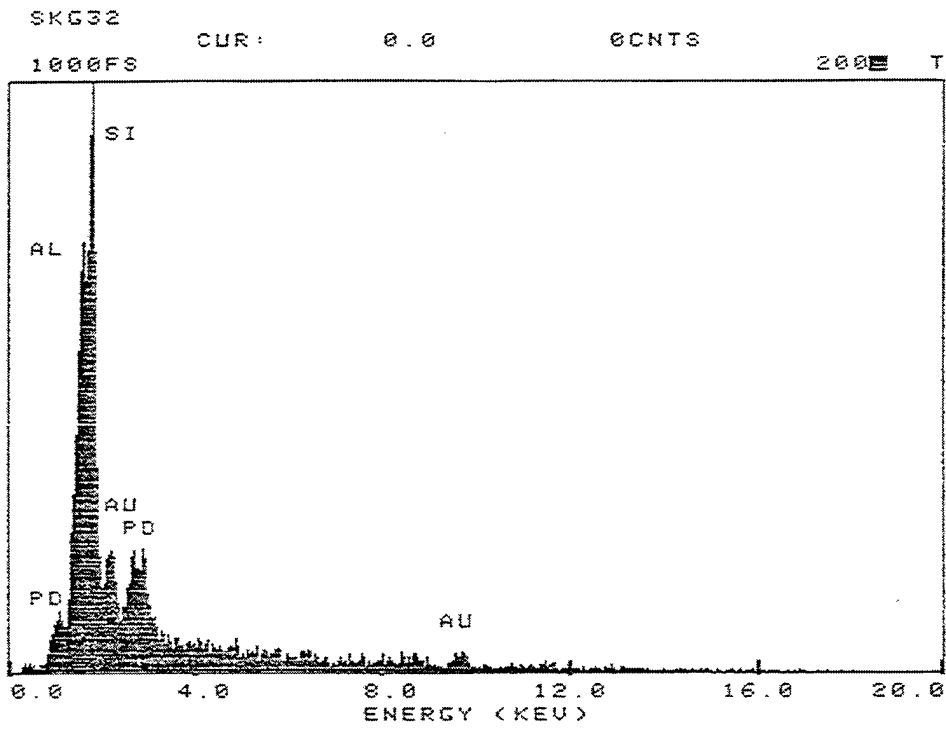


Figure 26

Figure 27 Overview of specimens present on stage 4 from shot 4

Notice the arrangement of the fine particles in a band extending from the upper left corner to the center of the right margin of the photograph. The band corresponds to the slot in the impactor stage directly above the Mylar substrate.

Figure 28 Details of specimens present on stage 4 from shot 4

Figure 29 X-ray energy dispersive spectrograph of the elemental composition of one of the particles illustrated in figure 28

The absence of tungsten from the specimen suggests that the target was the origin of the metal.

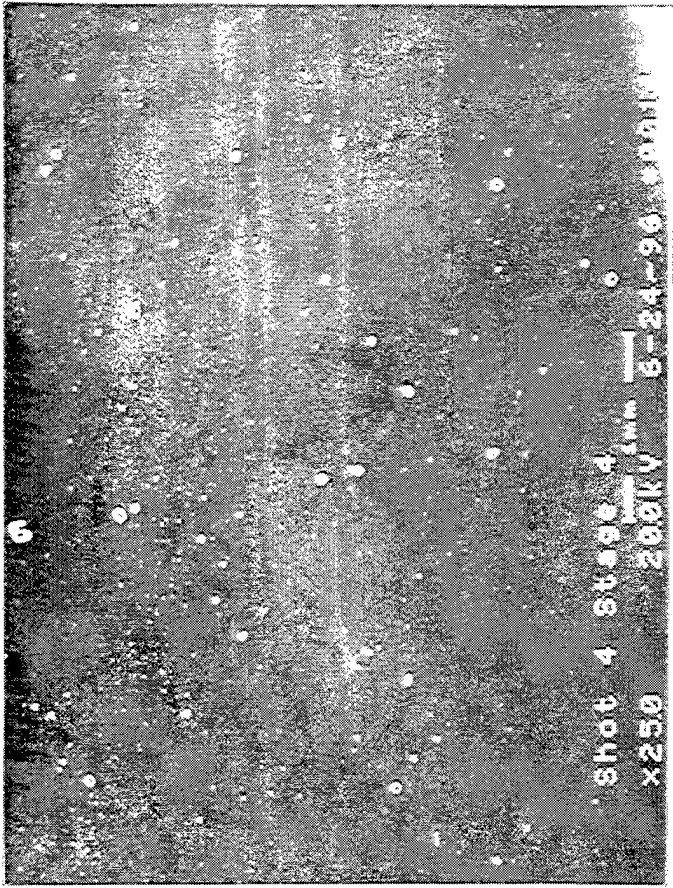


Figure 27

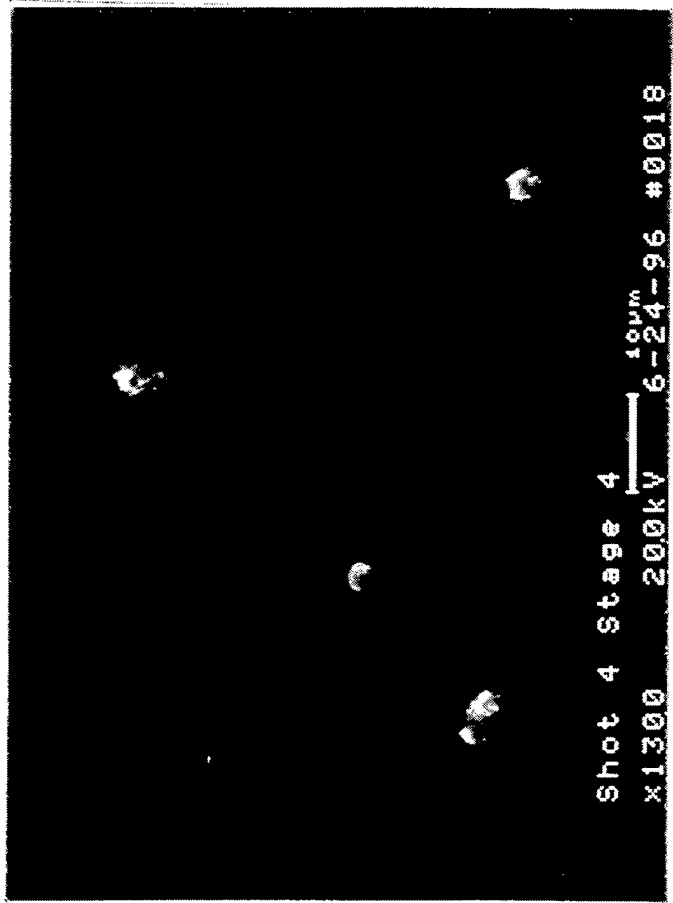


Figure 28

35

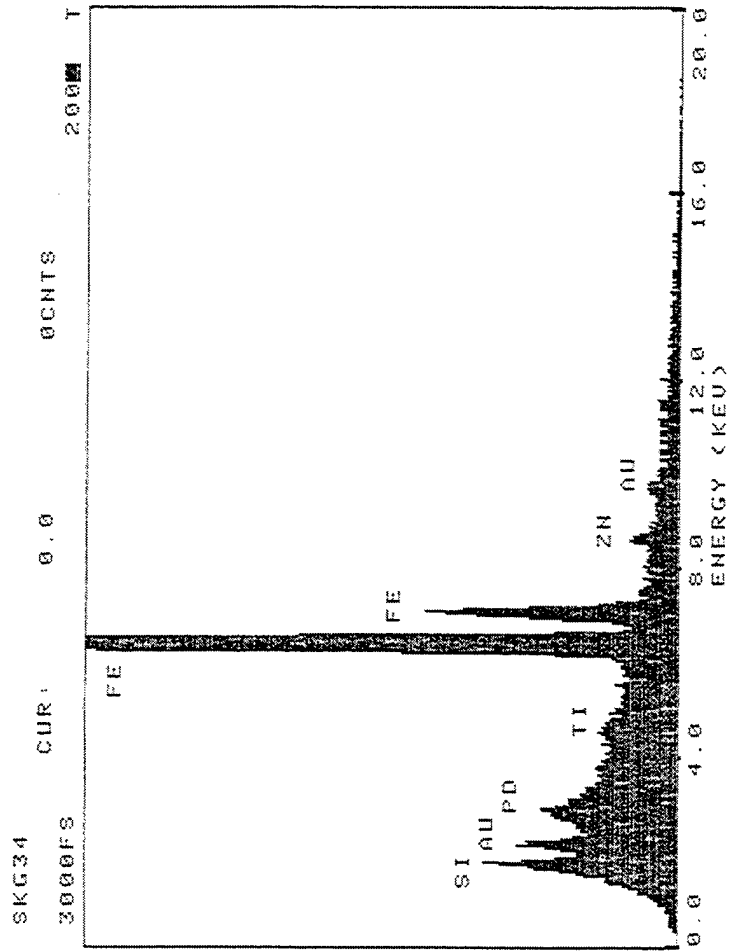


Figure 29

Figure 30 Overview of particles on stage 4 from shot 4

Figure 31 X-ray energy dispersive spectrograph of the elemental composition of one of the particles illustrated in figure 30 (arrow)
X-ray data was collected at high magnification.

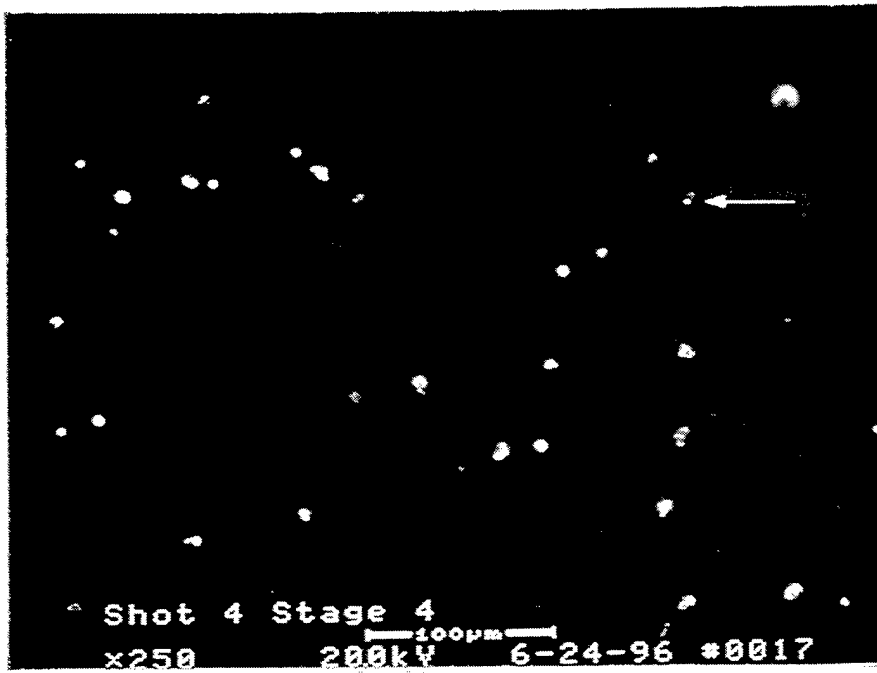


Figure 30

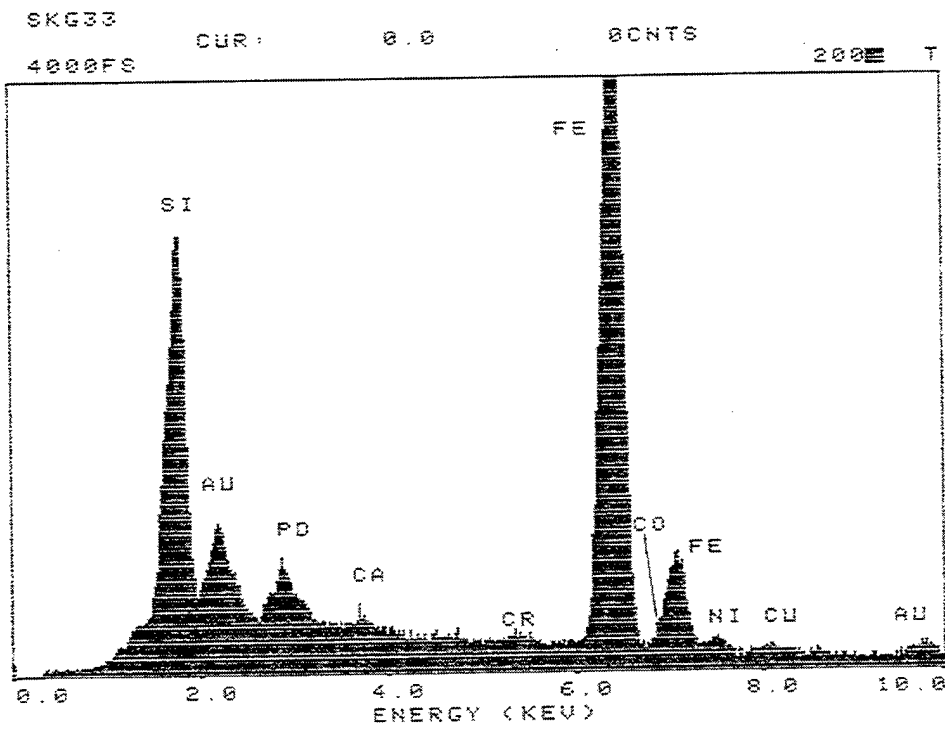


Figure 31

Figure 32 Overview of particles on stage 5 from shot 4

Figure 33 Details of particles on stage 5 from shot 4

Figure 34 X-ray energy dispersive spectrograph of the elemental composition of one of the particles illustrated in figure 33 (arrow)

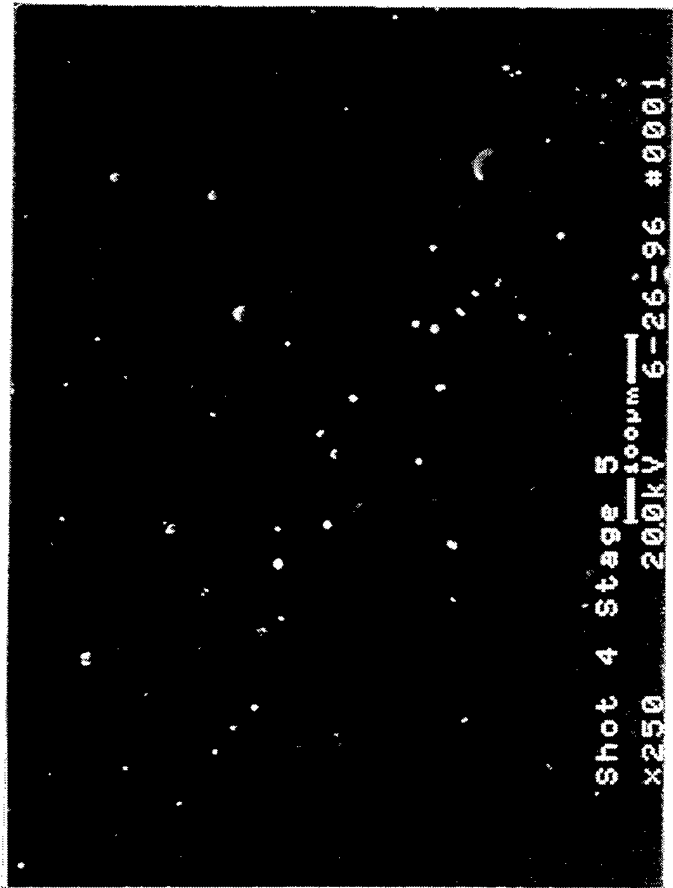


Figure 32

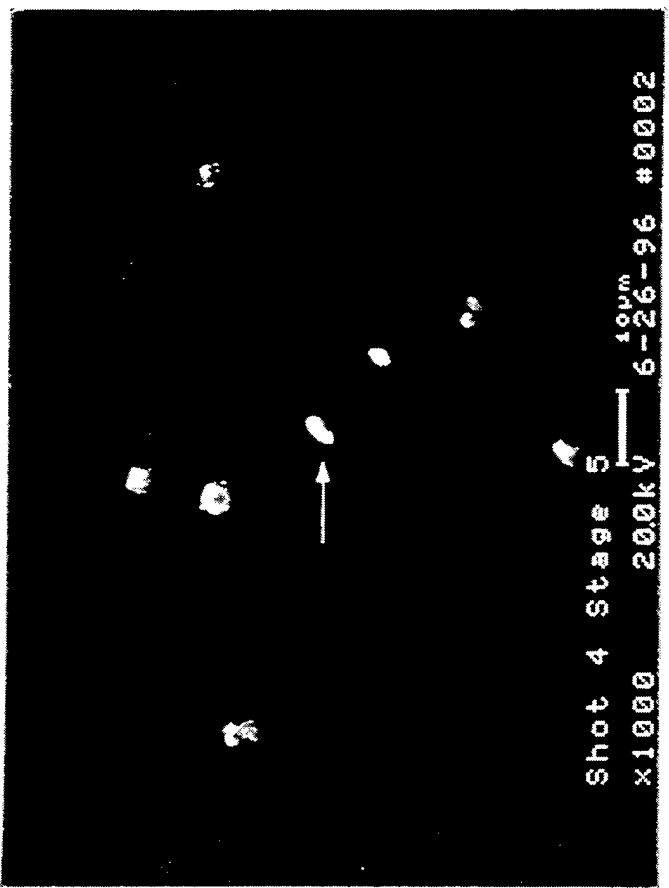


Figure 33

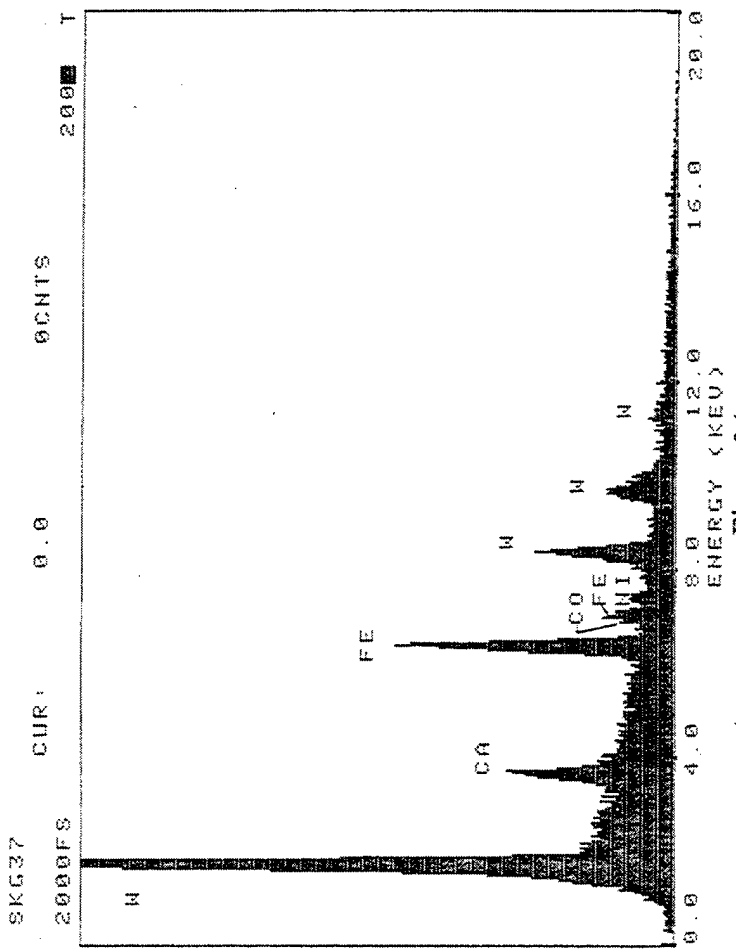


Figure 34

Figure 35 Overview of particles collected on stage 6 from shot 4

Figure 36 X-ray energy dispersive spectrograph of the elemental composition of one of the particles illustrated in figure 35
X-ray data was collected at high magnification



Figure 35

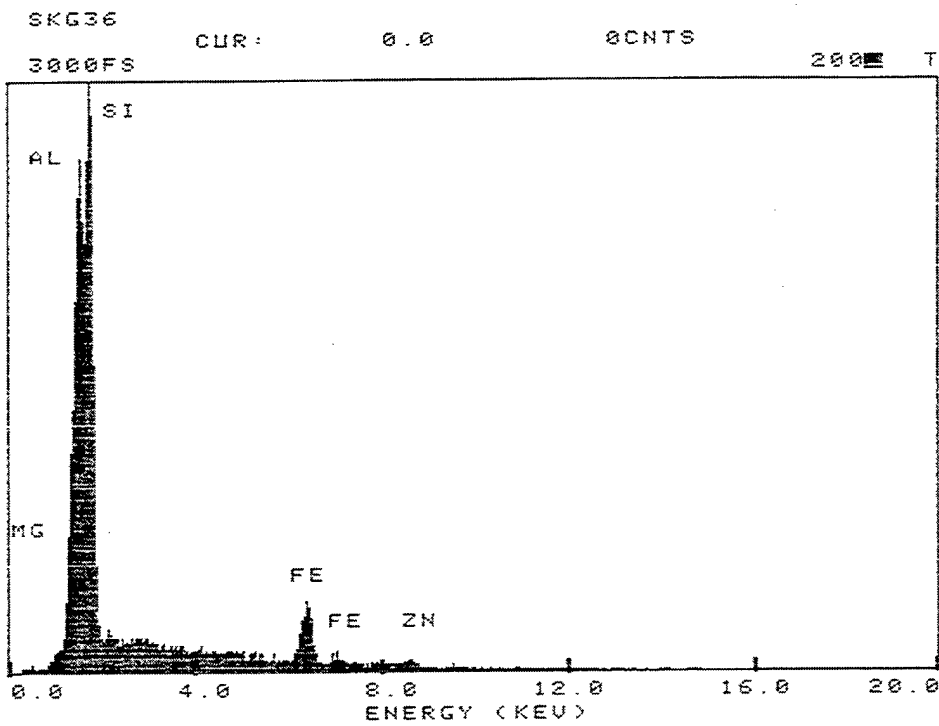


Figure 36

Figure 37 Overview of particles and agglomerations of particles on stage 8 from shot 4 (compare with figure 1)

Figure 38 Detail of a region illustrated in figure 37 (compare with figure 2)

Figure 39 X-ray energy dispersive spectrograph of the elemental composition of one of the agglomerations illustrated in figure 38

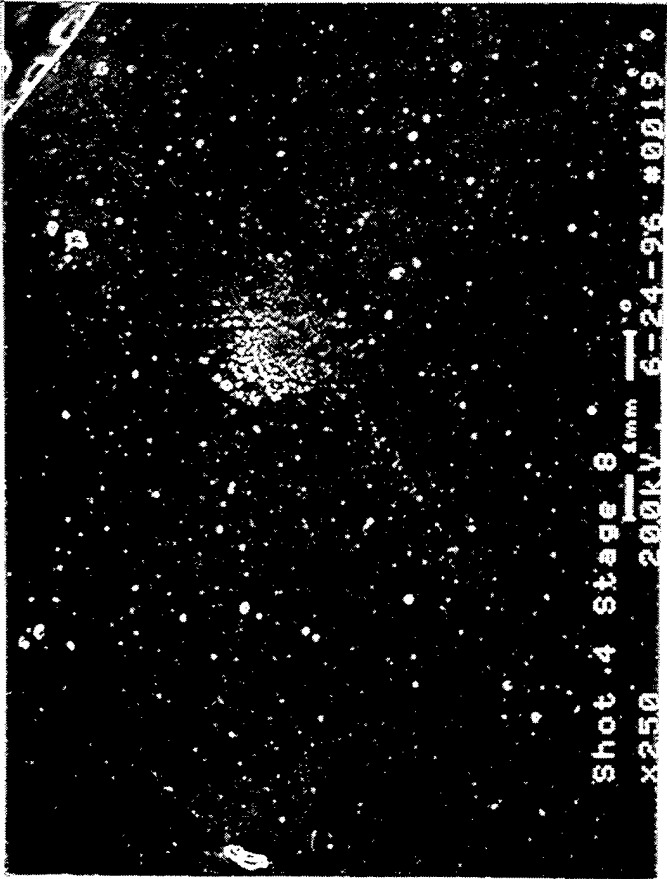


Figure 37



Figure 38

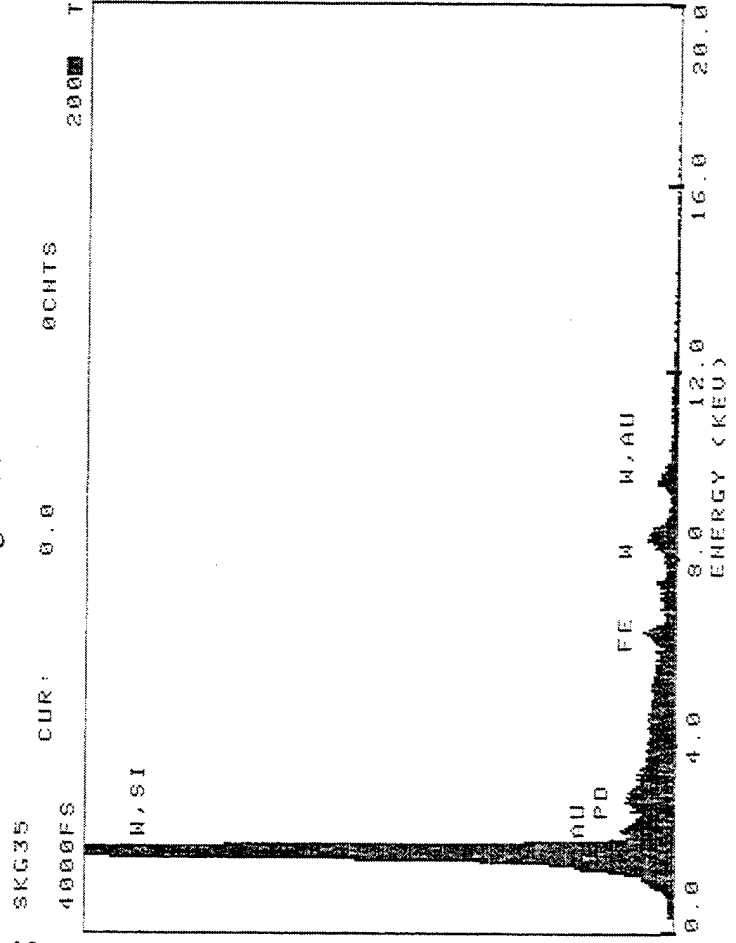


Figure 39

Figure 40 Dust particle (with satellites) retrieved from a cyclone collector

Figure 41 X-ray energy dispersive spectrograph of the elemental composition of the particle illustrated in figure 40



Figure 40

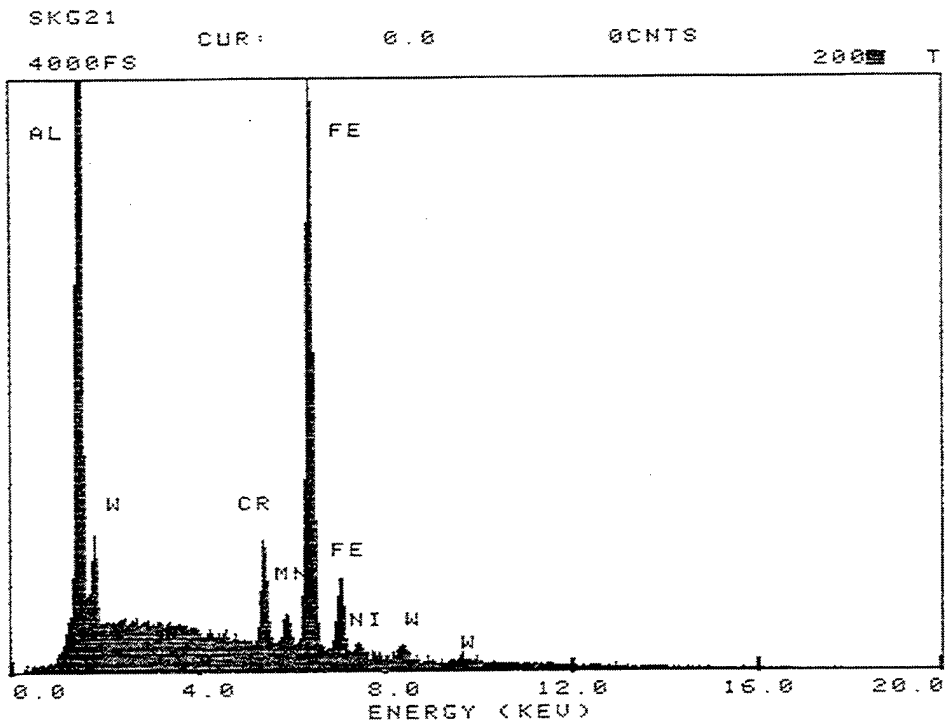


Figure 41

Figure 42 Fragment from the residue that remained on the test platform after a shot

Figure 43 Detail of the specimen illustrated in figure 42

Figure 44 X-ray energy dispersive spectrograph of the elemental composition of the fragment illustrated in figure 42

Note the aluminum peak and others attributable to both the penetrator and the target.

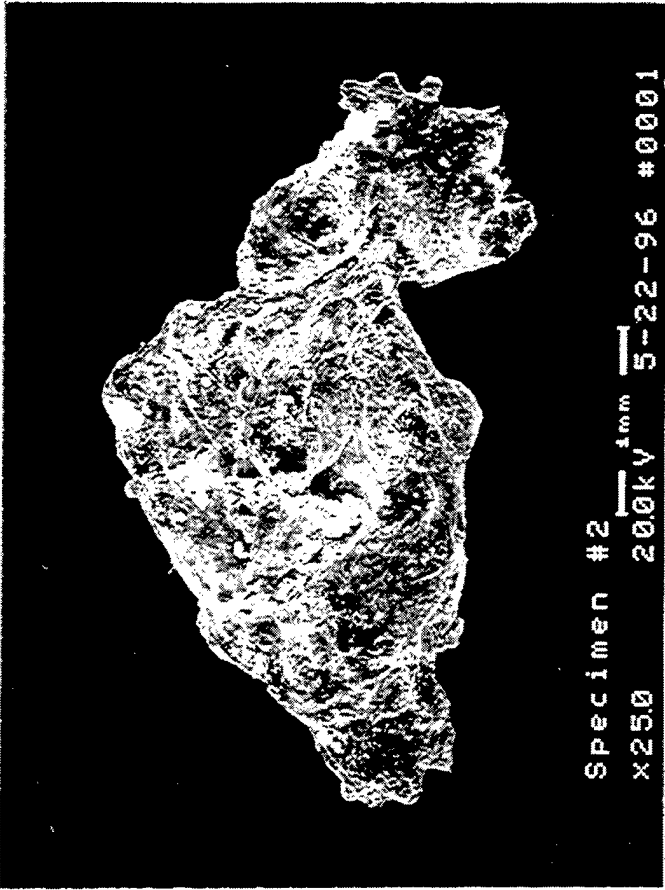


Figure 42



Figure 43

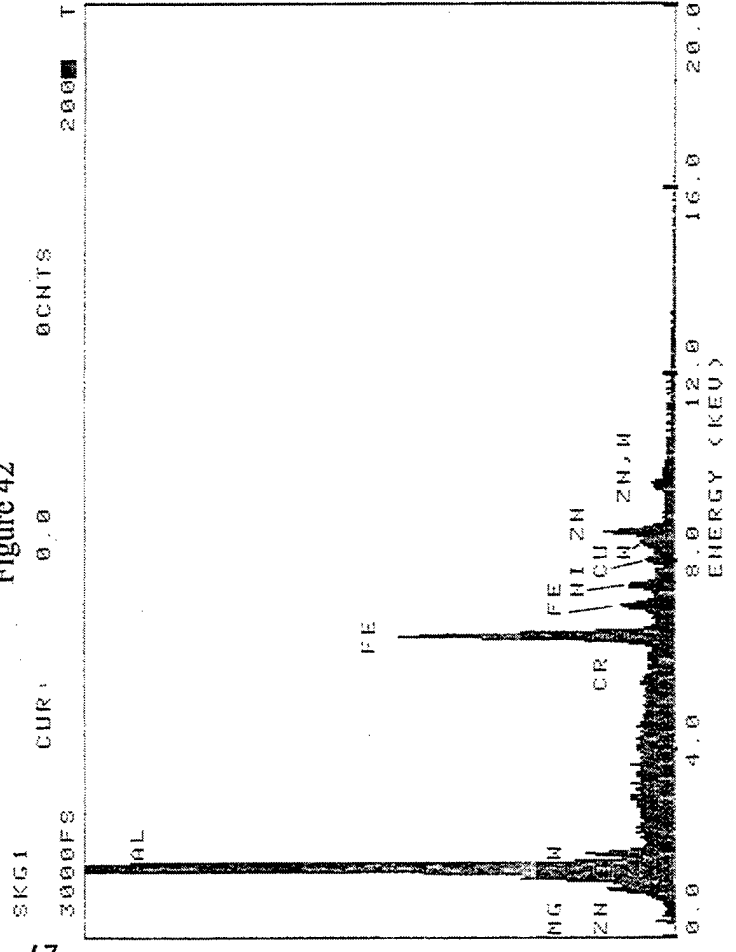


Figure 44

Figure 45 Specimen selected from the residue that remained on the test platform after a shot

Figure 46 Detail of the surface of the specimen shown in figure 45

Figure 47 X-ray energy dispersive spectrograph of the elemental composition of a region on the specimen illustrated in figures 45 and 46

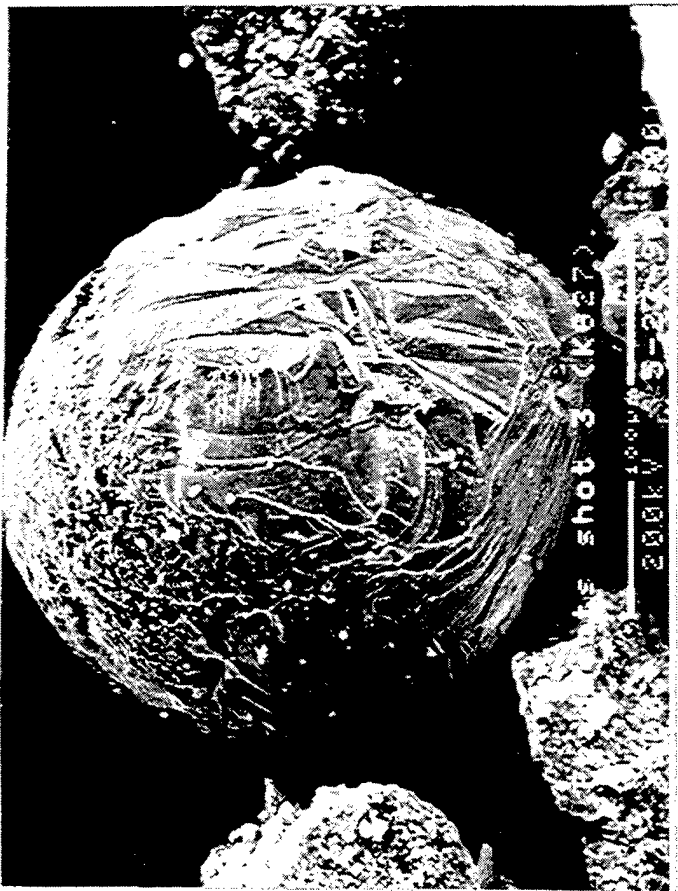


Figure 45

49



Figure 46

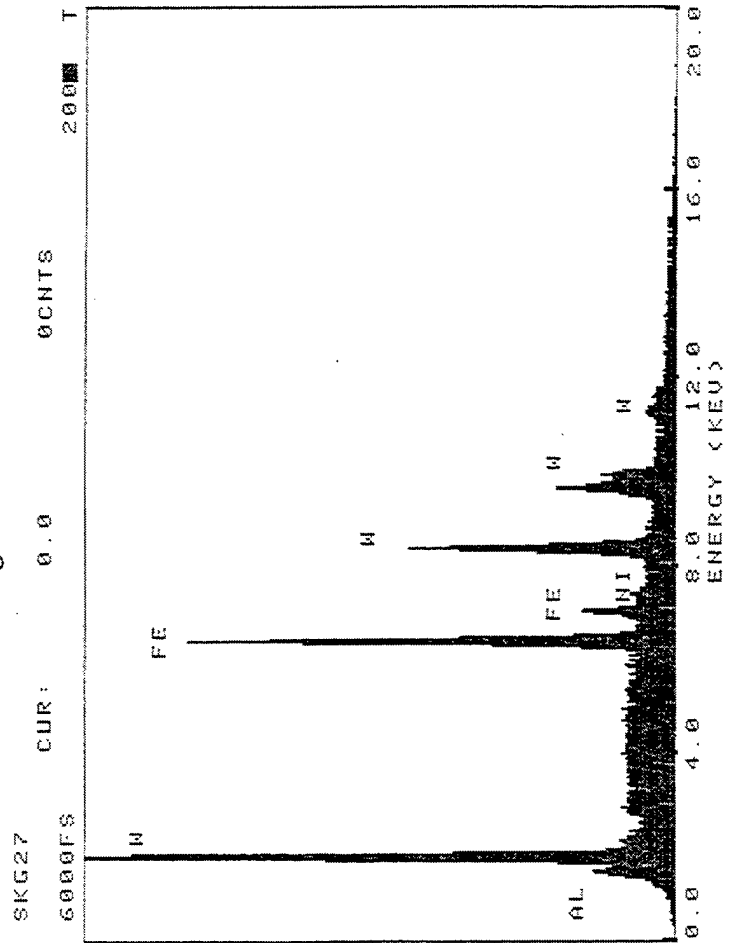


Figure 47

Figure 48 Specimen selected from the residue that remained on the test platform after a shot

Figure 49 X-ray energy dispersive spectrograph of the elemental composition of a region on the specimen illustrated in figure 48

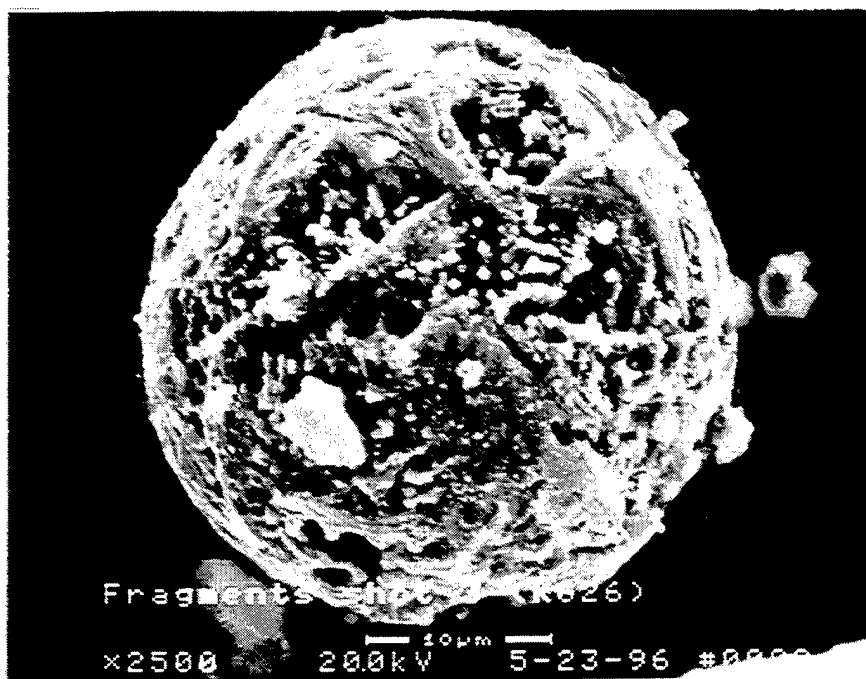


Figure 48

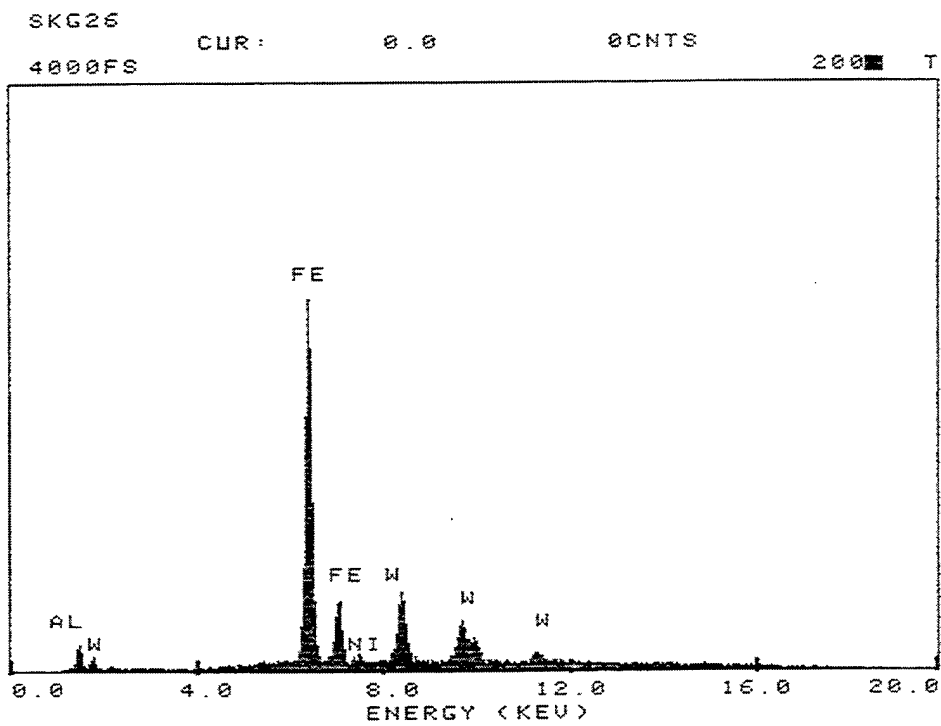


Figure 49

Figure 50 Specimen selected from the residue that remained on the test platform after a shot

Figure 51 X-ray energy dispersive spectrograph of the elemental composition of a region on the specimen illustrated in figure 50
The composition suggests the origin of the particle to be the penetrator with a possible contribution from the target.

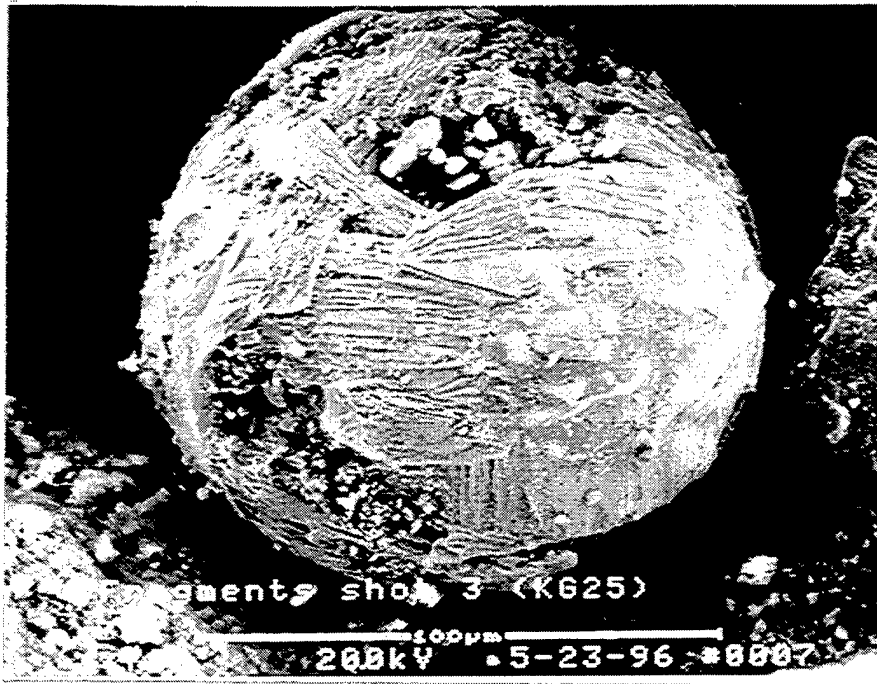


Figure 50

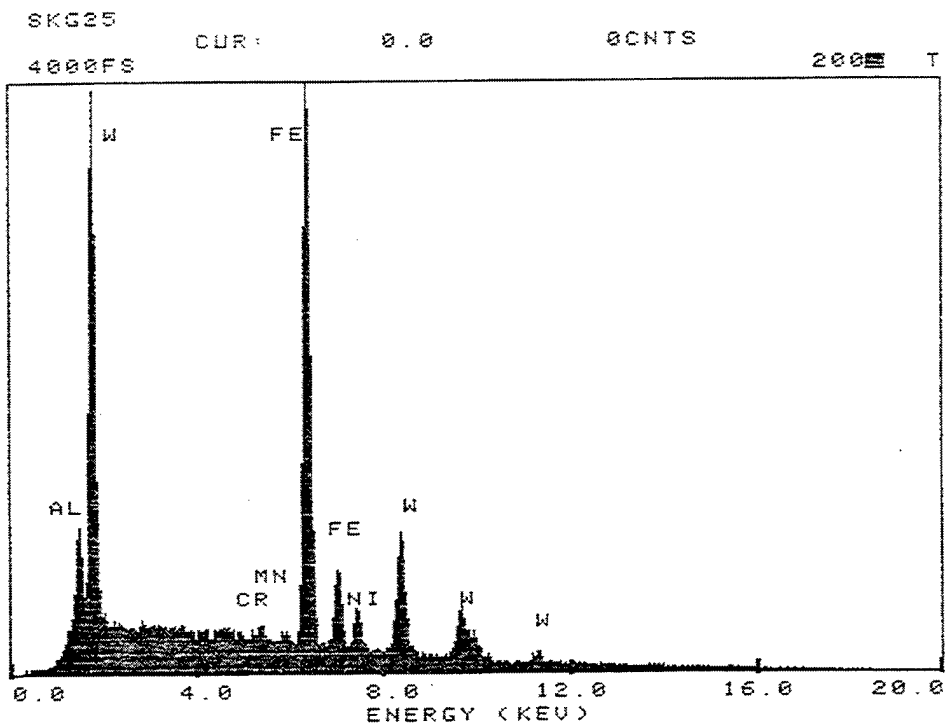


Figure 51

Figure 52 Specimen retrieved from a cyclone collector

Figure 53 X-ray energy dispersive spectrograph of the elemental composition of a region on the specimen illustrated in figure 52

The composition suggests the origin of the particle to be the target.

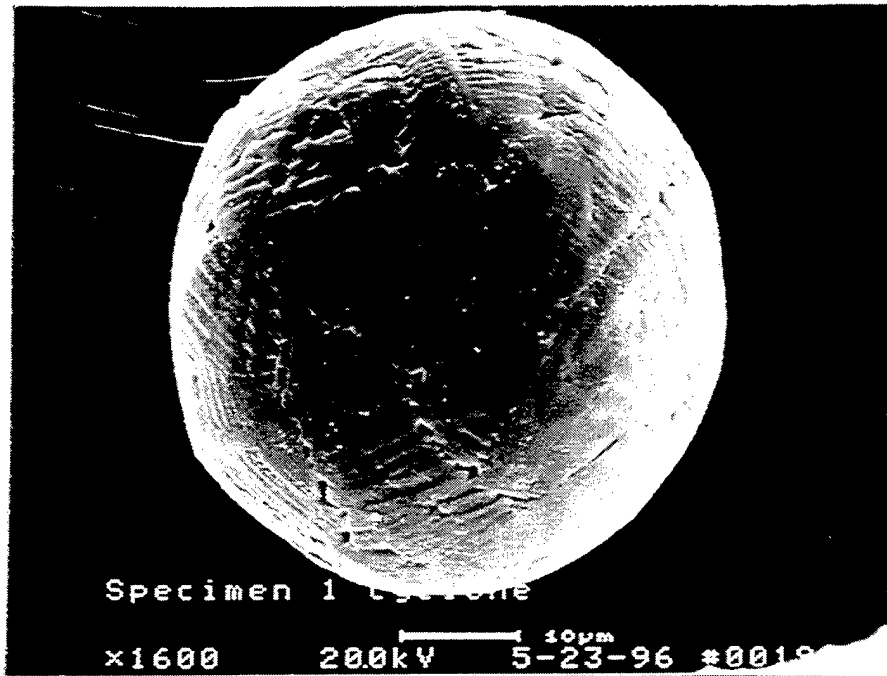


Figure 52

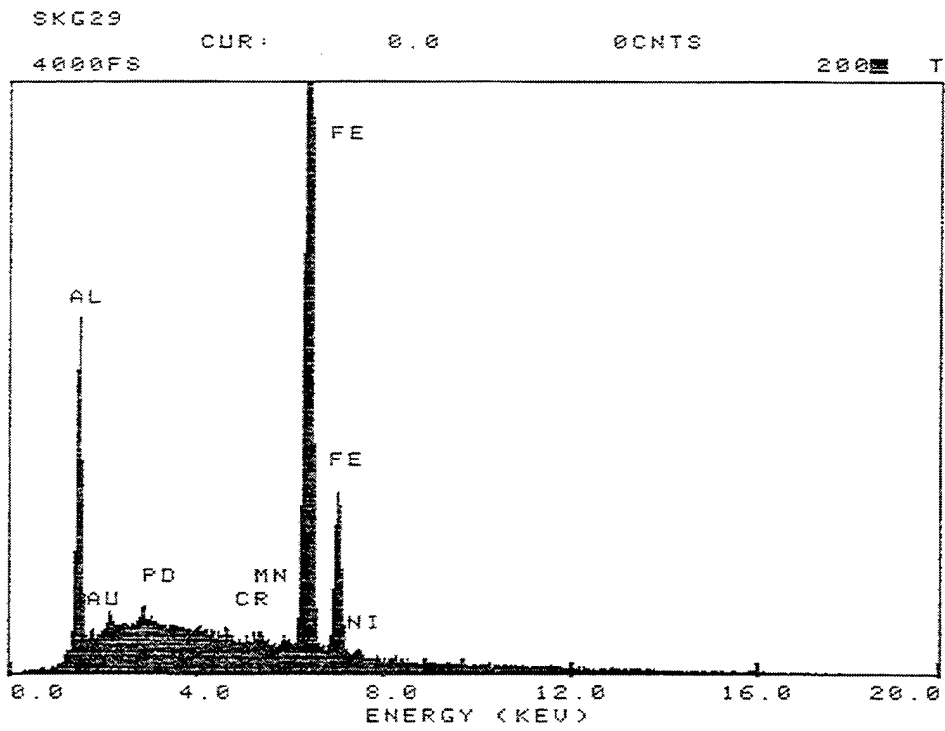


Figure 53

Figure 54 Fragment selected from the residue that remained on the test platform after a shot

Figure 55 X-ray energy dispersive spectrograph of the elemental composition of a region on the particle illustrated in figure 54
The composition suggests the origin of the particle to be the target.

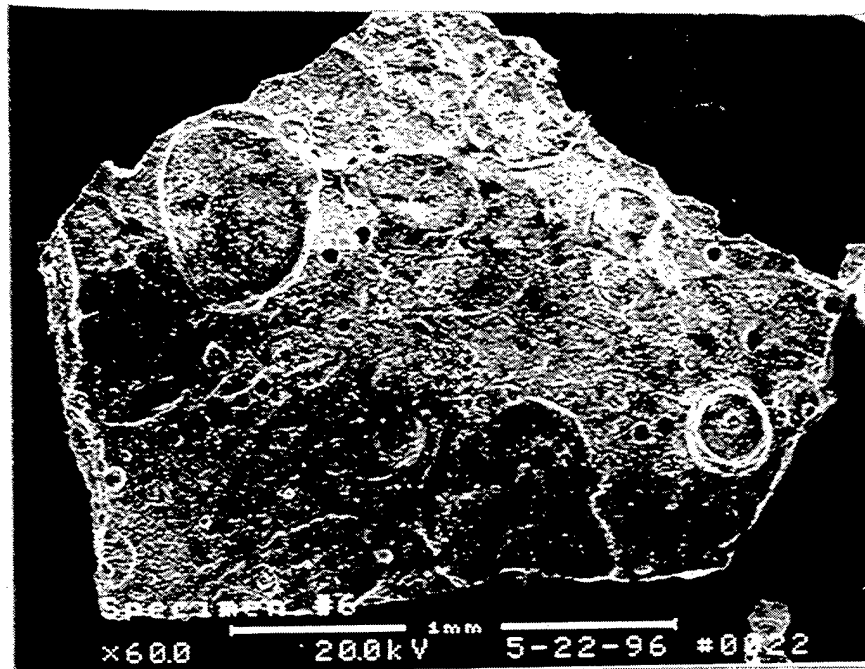


Figure 54

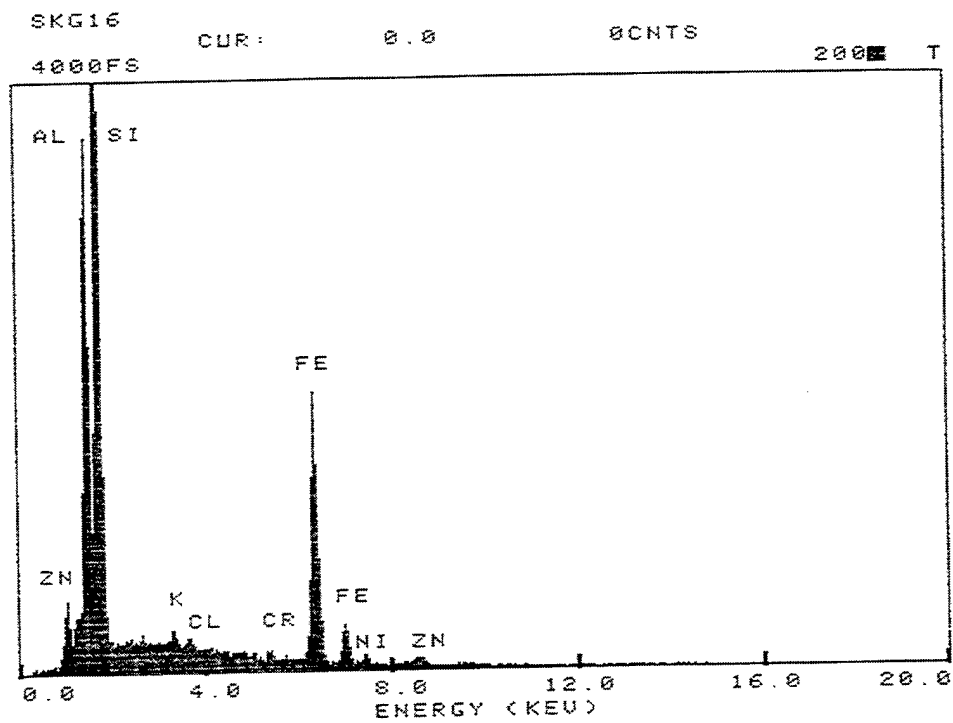


Figure 55

Figure 56 Fragment selected from the residue that remained on the test platform after a shot

Figure 57 X-ray energy dispersive spectrograph of the elemental composition of a region on the fragment illustrated in figure 56
The composition suggests the origin of the particle to be the penetrator.

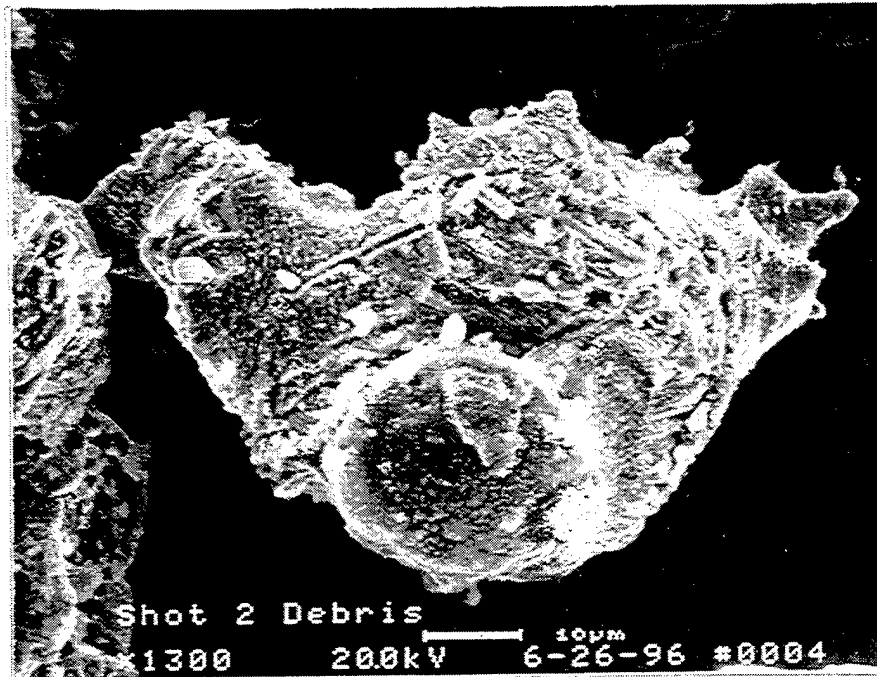


Figure 56

SKG38 CUR: 0.0 GCNTS 200 T
 4000FS

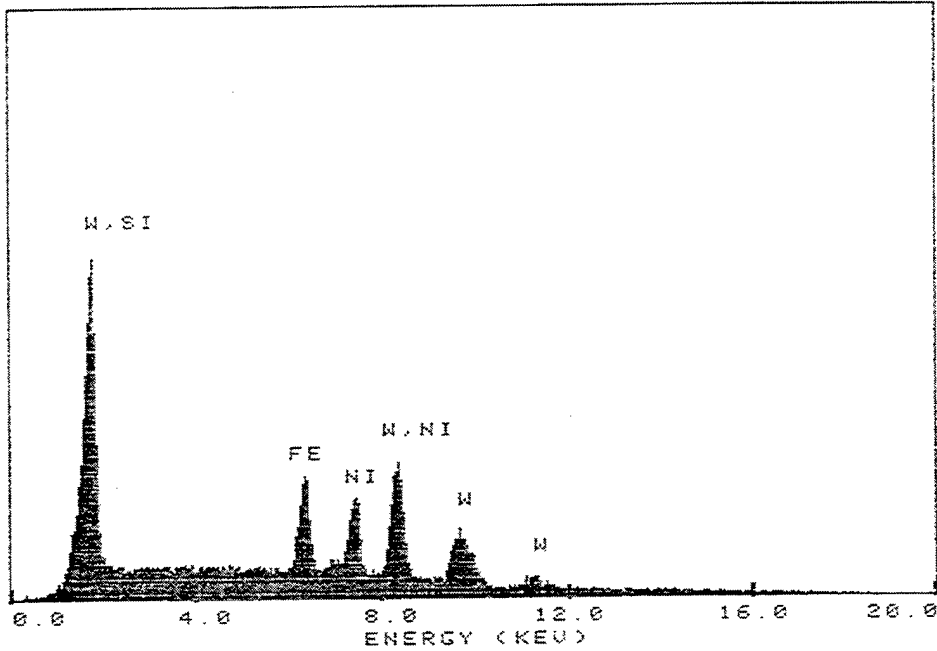


Figure 57

REFERENCES

1. Gold, K. and Los, M., "Environment Analysis of Tungsten Alloy Penetrators: Manufacturing and Testing Phases of the Life Cycle," U.S. Army Armament Research, Development and Engineering Center, Production Base Modernization Activity, Picatinny Arsenal, NJ, May 1996.
2. Jette, S. J.; Mishima, J.; Hadlock, D. E., "Aerosolization of the M829A1 and XM900E1 Rounds Fires Against Hard Targets," Technical Report PNL-7452, Pacific Northwest Laboratory, Richland, WA, 1990.
3. U.S. Department of Health and Human Services, Public Health Services, Criteria for a Recommended Standard... Occupational Exposure to Tungsten and Cemented Tungsten Carbide, NIOSH Publication No. 77-127, Public Health Services, National Institute for Occupational Safety and Health (NIOSH), September 1977.
4. Kanapilly, G. M.; Raabe, O. G.; Goh, C. H. T.; and Chimenti, R. A., "Measurement of In-vitro Dissolution of Aerosol Particles for Comparison in In-vitro Dissolution in the Lower Respiratory Tract After Inhalation," Health Physics, Vol. 24, pp 497-507, 1973.
5. Cooke, N. and Holt, F. B., "The Solubility of Some Uranium Compounds in Simulated Lung Fluid," Health Physics, Vol. 27, pp. 69-77.
6. Instruction Manual, Series 290 Marple Personal Cascade Impactors, Sierra Technical Bulletin No. 290I.M-3-82.
7. Gold, K., unpublished data.
8. Magness, L. S. and Farrand, T. G., "Deformation Behavior and It's Relationship to the Penetration Performance of High-Density KE Penetrator Materials," Proceedings, Army Science Conference, Durham, NC, Vol. 2, 465-479, 1990.
9. Gerlach, U., "Microstructural Analysis of Residual Projectiles—A New Method to Explain Penetration Mechanisms," Metallurgical Transactions A, Vol. 17A, pp 435-442, 1986.
10. Li, K. C. and Wang, C. Y., Tungsten, It's History, Geology, Ore-Dressing, Metallurgy, Chemistry, Analysis, Applications, and Economics, Reinhold Publishing Corporation, New York, 1955.
11. Hagrman, D. L.; Smolik, G. R.; Petti, D. A.; McCarthy, K. A., "Oxide Aerosols Produced from a Tungsten Alloy for Fusion Reactors," Fusion Technology, Vol. 26, pp 993-997, 1994.

REFERENCES (cont)

12. Smolik, G. R.; Piet, S. J.; and Neilson, R. M., Jr., "Predictions of Radioactive Tungsten Release for Hypothetical ITET Accidents," Fusion Technology, Vol. 19, pp 1398-1402, 1991.
13. Chung, M. and Gold, K., unpublished, 1996.

APPENDIX A

TABLES

Table A-1
 Meteorological and sample collection data

Shot No.	Date	Shot time	Humidity (%)	Wind speed (mph)	Temp (°F)	Impactor position/no.	Flow rate (L/min)	Total flow (L)
1	15 Apr 96	13:25	50	13-17	50	Right R7197	3.90	11.7
						Right T7457	4.10	12.3
						Left K7193	4.00	12.0
2	15 Apr 96	15:22	55	15-22	49	Right W1041	3.90	19.5
						Right W1040	4.10	20.5
						Left W1042	4.00	20.0
3	16 Apr 96	15:00	47	2-18	55	Left W1043	2.00	10.0
						Right W1045	2.04	10.2
						Left Back W1044	2.14	10.7
4	17 Apr 96	09:55	43	12-22	46	Left W0907	2.14	10.7
						Right W0908	2.06	10.3
						Left Back T8323	2.13	10.7
5	17 Apr 96	11:13	41	12-22	47	Left W4498	2.14	10.7
						Right T2012	2.00	10.3
						Left Back T7457	2.13	10.7
6	17 Apr 96	14:00	30	14-24	51	Left R7193	2.14	10.7
						Right W1041	2.06	10.3
						Left Back R7197	2.13	10.7

Table A-2
Cascade impactor data, shot 1a

Test Date: 15 Apr 96
Shot No: 1a
Impactor No.: R7197

Location: Right Side
Sample Vol.: 11.70 L
Sample ID: 16089

Stage	Cut point (μ)	Particle weight (mg)	Conc. (mg/m^3)
1	16.25	0.03	3
2	10.50	0.00	0
3	6.75	0.00	0
4	4.10	0.12	10
5	2.50	0.00	0
6	0.98	0.01	1
7	0.64	0.01	1
8	0.35	0.02	2
Backup filter	0.25	0.01	1

Table A-3
Cascade impactor data, shot 1b

Test Date: 15 Apr 96
Shot No: 1b
Impactor No.: T7457

Location: Right Side
Sample Vol.: 12.30 L
Sample ID: 16090

Stage	Cut point (μ)	Particle weight (mg)	Conc. (mg/m^3)
1	16.25	0.11	9
2	10.50	0.00	0
3	6.75	0.00	0
4	4.10	0.00	0
5	2.50	0.00	0
6	0.98	0.00	0
7	0.64	0.00	0
8	0.35	0.00	0
Backup filter	0.25	0.01	1

Table A-4
Cascade impactor data, shot 1c

Test Date: 15 Apr 96
Shot No: 1c
Impactor No.: R7193

Location: Left Side
Sample Vol.: 12.00 L
Sample ID: 16091

Stage	Cut Point (μ)	Particle Weight (mg)	Conc. (mg/m^3)
1	16.25	1.22	102
2	10.50	0.00	0
3	6.75	0.01	1
4	4.10	0.01	1
5	2.50	0.00	0
6	0.98	0.00	0
7	0.64	0.00	0
8	0.35	0.00	0
Backup filter	0.25	0.03	3

Table A-5
Cascade impactor data, shot 2a

Test Date: 15 Apr 96
Shot No.: 2a
Impactor No.: W1041

Location: Right Side
Sample Vol.: 19.50
Sample ID: 16092

Stage	Cut Point (μ)	Particle Weight (mg)	Conc. (mg/m^3)
1	16.25	0.23	12
2	10.50	0.07	4
3	6.75	0.00	0
4	4.10	0.00	0
5	2.50	0.00	0
6	0.98	0.00	0
7	0.64	0.00	0
8	0.35	0.00	0
Backup filter	0.25	0.05	3

Table A-6
Cascade impactor data, shot 2b

Test Date: 15 Apr 96
Shot No: 2b
Impactor No.: W1040

Location: Right Side
Sample Vol.: 20.50 L
Sample ID: 16093

Stage	Cut point (μ)	Particle weight (mg)	Conc. (mg/m^3)
1	16.25	0.30	15
2	10.50	0.03	1
3	6.75	0.00	0
4	4.10	0.00	0
S	2.50	0.00	0
6	0.98	0.00	0
7	0.64	0.00	0
8	0.35	0.00	0
Backup filter	0.25	0.01	0

Table A-7
Cascade impactor data, shot 2c

Test Date: 15 Apr 96
Shot No: 2c
Impactor No.: W1042

Location: Left Side
Sample Vol.: 20.00 L
Sample ID: 16094

Stage	Cut point (μ)	Particle weight (mg)	Conc. (mg/m^3)
1	16.25	0.20	10
2	10.50	0.12	6
3	6.75	0.18	9
4	4.10	0.00	0
5	2.50	0.00	0
6	0.98	0.00	0
7	0.64	0.00	0
8	0.35	0.00	0
Backup filter	0.25	0.00	0

Table A-8
Cascade impactor data, shot 3a

Test Date: 16 Apr 96
Shot No: 3a
Impactor No.: W1043

Location: Left Side
Sample Vol.: 10.00 L
Sample ID: 16095

Stage	Cut point (μ)	Particle weight (mg)	Conc. (mg/m^3)
1	21	0.05	5
2	15	0.00	0
3	10	0.00	0
4	6	0.00	0
5	3.5	0.00	0
6	2	0.00	0
7	0.9	0.00	0
8	0.5	0.00	0
Backup filter	0.25	0.02	2

Table A-9
Cascade impactor data, shot 3b

Test Date: 16 Apr 96
Shot No: 3b
Impactor No.: W1045

Location: Right Side
Sample Vol.: 10.20 L
Sample ID: 16096

Stage	Cut point (μ)	Particle weight (mg)	Conc. (mg/m^3)
1	21	0.00	0
2	15	0.00	0
3	10	0.00	0
4	6	0.00	0
5	3.5	0.00	0
6	2	0.00	0
7	0.9	0.00	0
8	0.5	0.00	0
Backup filter	0.25	0.01	1

Table A-10
Cascade impactor data, shot 3c

Test Date: 16 Apr 96
Shot No: 3c
Impactor No.: W1044

Location: Left Back
Sample Vol.: 10.65 L
Sample ID: 16097

Stage	Cut point (μ)	Particle weight (mg)	Conc. (mg/m^3)
1	21	0.00	0
2	15	0.00	0
3	10	0.00	0
4	6	0.00	0
5	3.5	0.00	0
6	2	0.00	0
7	0.9	0.00	0
8	0.5	0.00	0
Backup filter	0.25	0.01	1

Table A-11
Cascade impactor data, shot 4a

Test Date: 17 Apr 96
Shot No: 4a
Impactor No.: W0907

Location: Left Side
Sample Vol.: 10.70 L
Sample ID: 16098

Stage	Cut point (μ)	Particle weight (mg)	Conc. (mg/m^3)
1	21	0.06	6
2	15	0.00	0
3	10	0.01	1
4	6	0.00	0
5	3.5	0.00	0
6	2	0.00	0
7	0.9	0.00	0
8	0.5	0.00	0
Backup filter	0.25	0.00	0

Table A-12
Cascade impactor data, shot 4b

Test Date: 17 Apr 96
Shot No: 4b
Impactor No.: W0908

Location: Right Side
Sample Vol.: 10.30 L
Sample ID: 16099

Stage	Cut point (μ)	Particle weight (mg)	Conc. (mg/m ³)
1	21	0.03	3
2	15	0.00	0
3	10	0.00	0
4	6	0.00	0
5	3.5	0.00	0
6	2	0.00	0
7	0.9	0.00	0
8	0.5	0.00	0
Backup filter	0.25	0.02	2

Table A-13
Cascade impactor data, shot 4c

Test Date: 17 Apr 96
Shot No: 4c
Impactor No.: T8323

Location: Left Back
Sample Vol.: 10.65 L
Sample ID: 16100

Stage	Cut point (μ)	Particle weight (mg)	Conc. (mg/m ³)
1	21	0.26	24
2	15	0.06	6
3	10	0.03	3
4	6	0.00	0
5	3.5	0.00	0
6	2	0.00	0
7	0.9	0.00	0
8	0.5	0.00	0
Backup filter	0.25	0.03	3

Table A-14
 Cascade impactor data, shot 5a

Test Date: 17 Apr 96
 Shot No: 5a
 Impactor No.: W4498

Location: Left Side
 Sample Vol.: 10.70 L
 Sample ID: 16101

Stage	Cut point (μ)	Particle weight (mg)	Conc. (mg/m^3)
1	21	0.02	2
2	15	0.00	0
3	10	0.01	1
4	6	0.00	0
5	3.5	0.00	0
6	2	0.00	0
7	0.9	0.01	1
8	0.5	0.00	0
Backup filter	0.25	0.03	3

Table A-15
 Cascade impactor data, shot 5b

Test Date: 17 Apr 96
 Shot No: 5b
 Impactor No.: T2012

Location: Right Side
 Sample Vol.: 10.30 L
 Sample ID: 16102

Stage	Cut point (μ)	Particle weight (mg)	Conc. (mg/m^3)
1	21	0.00	0
2	15	0.00	0
3	10	0.00	0
4	6	0.00	0
5	3.5	0.00	0
6	2	0.00	0
7	0.9	0.00	0
8	0.5	0.00	0
Backup filter	0.25	0.01	1

Table A-16
 Cascade impactor data, shot 5c

Test Date: 17 Apr 96
 Shot No.: 5c
 Impactor No.: T7457

Location: Left Back
 Sample Vol.: 10.65
 Sample ID: 16103

Stage	Cut point (μ)	Particle weight (mg)	Conc. (mg/m^3)
1	21	0.00	0
2	15	0.00	0
3	10	0.00	0
4	6	0.00	0
5	3.5	0.00	0
6	2	0.00	0
7	0.9	0.00	0
8	0.5	0.00	0
Backup filter	0.25	0.01	1

Table A-17
 Cascade impactor data, shot 6a

Test Date: 17 Apr 96
 Shot No: 6a
 Impactor No.: R7193

Location: Left Side
 Sample Vol.: 10.70 L
 Sample ID: 16104

Stage	Cut point (μ)	Particle weight (mg)	Conc. (mg/m^3)
1	21	0.12	11
2	15	0.00	0
3	10	0.00	0
4	6	0.00	0
5	3.5	0.00	0
6	2	0.00	0
7	0.9	0.00	0
8	0.5	0.00	0
Backup Filter	0.25	0.04	4

Table A-18
Cascade impactor data, shot 6b

Test Date: 17 Apr 96
Shot No.: 6b
Impactor No.: W1041

Location: Right Side
Sample Vol.: 10.30 L
Sample ID: 16105

Stage	Cut point (μ)	Particle weight (mg)	Conc. (mg/m ³)
1	21	0.01	1
2	15	0.00	0
3	10	0.00	0
4	6	0.01	1
5	3.5	0.00	0
6	2	0.00	0
7	0.9	0.00	0
8	0.5	0.00	0
Backup filter	0.25	0.01	1

Table A-19
Cascade impactor data, shot 6c

Test Date: 17 Apr 96
Shot No.: 6c
Impactor No.: R7197

Location: Left Back
Sample Vol.: 10.65 L
Sample ID: 16106

Stage	Cut point (μ)	Particle weight (mg)	Conc. (mg/m ³)
1	21	0.00	0
2	15	0.00	0
3	10	0.00	0
4	6	0.01	1
5	3.5	0.00	0
6	2	0.00	0
7	0.9	0.00	0
8	0.5	0.00	0
Backup filter	0.25	0.03	3

Table A-20
 Quantitative analysis of aerosols
 [calculated values for nickel (in air)]

Shot-unit ID	Flow vol (L)	Stages	mg/m ³ in air
#2-4	19.5	1-3	0.373
#2-5	20.5	1-3	0/868
#4-3	10.7	4-5	0.079

Table A-21
 Quantitative analysis of aerosols
 [calculated values for tungsten (in air)]

Shot-unit ID	Flow vol (L)	Stages	mg/m ³ in air
#1-3	11.7	1-3	0.064
#2-4	19.5	1-3	0.068
#3-W1044	10.7	8	0.135
#6-4	10.7	1-3	0.053

Table A-22
 Quantitative analysis of aerosols
 [calculated values for iron (in air)]

Shot-unit ID	Flow vol (L)	Stages	mg/m ³ in air
1-3	11.7	1-3	1.297
1-3	11.7	4-5	0.1
1-3	11.7	8	0.041
1-3	11.7	CE filter	0.13
1-4	12.3	1-3	3.606
1-4	12.3	4-5	0.315
1-4	12.3	6-7	0.087
2-4	19.5	4-5	0.104
2-4	19.5	6-7	0.068
2-4	19.5	8	0.099
2-4	19.5	CE filter	0.051
2-5	20.5	1-3	10.255
2-5	20.5	4-5	0.037
2-5	20.5	6-7	0.03
2-5	20.5	8	0.029
3-W1044	10.7	1-3	0.194
3-W1044	10.7	4-5	0.086
3-W1044	10.7	6-7	0.084
3-W1044	10.7	CE filter	0.084
3-W1045	10.2	1-3	0.846
3-W1045	10.2	4-5	0.049
3-W1045	10.2	6-7	0.044
3-W1045	10.2	8	0.127
3-W1045	10.2	CE filter	0.086
4-3	10.7	1-3	1.488
4-3	10.7	4-5	0.734
4-3	10.7	6-7	0.091
4-3	10.7	8	0.061

Table A-22
(cont)

Shot-unit ID	Flow vol. (L)	Stages	mg/m ³ in air
4-3	10.7	CE filter	0.084
4-4	10.3	1-3	0.252
4-4	10.3	CE filter	0.044
5-4	10.7	1-3	0.439
5-4	10.7	6-7	0.075
5-4	10.7	CE filter	0.079
5-5	10.3	1-3	0.272
5-5	10.3	4-5	0.417
5-5	10.3	6-7	0.053
5-5	10.3	CE filter	0.063
6-4	10.7	1-3	0.329
6-4	10.7	4-5	0.065
6-4	10.7	6-7	0.082
6-4	10.7	8	0.079
6-5	10.3	1-3	0.206
6-5	10.3	4-5	0.08
6-5	10.3	6-7	0.07
6-5	10.3	8	0.245
6-5	10.3	CE filter	0.056

DISTRIBUTION LIST

Commander
Armament Research, Development and Engineering Center
U.S. Army Tank-automotive and Armaments Command
ATTN: AMSTA-AR-WEL-TL (2)
AMSTA-AR-GLC
AMSTA-AR-AET-M, D. Kapoor
M. Chung
K. Willison
M. Mortman
AMSTA-AR-CCH-A, M. Nicolich
Picatinny Arsenal, NJ 07806-5000

Director
Systems Readiness Center
ATTN: AMSTA-AR-SRE
AMSTA-AR-SRE, D. W. Yee
K. Gold (25)
M. Los
Picatinny Arsenal, NJ 07806-5000

Project Manager
Tank Main Armament System
ATTN: SFAE-ASM-TMA-PA, V. Rosamilia
E. Kopacz
SFAE-ASM-TMA-MS, C. Roller
R. T. Kowalski
SFAE-ASM-TMA-SM, B-354, D. Guziewicz
Picatinny Arsenal, NJ 07806-5000

Defense Technical Information Center (DTIC)
ATTN: DTIC-OCC (12)
8725 John J. Kingman Road, Ste 0944
Fort Belvoir, VA 22060-6218

Director
U.S. Army Materiel Systems Analysis Activity
ATTN: AMXSU-MP
Aberdeen Proving Ground, MD 21010-5423

Commander
Chemical/Biological Defense Agency
U.S. Army Armament, Munitions and Chemical Command
ATTN: AMSCB-CII, Library
Aberdeen Proving Ground, MD 21010-5423

Director
U.S. Army Edgewood Research, Development and Engineering Center
ATTN: SCBRD-RTB (Aerodynamics Technology Team)
Aberdeen Proving Ground, MD 21010-5423

Director
U.S. Army Research Laboratory
ATTN: L. S. Magness
AMSRL-OP-CI-B, Technical Library
Aberdeen Proving Ground, MD 21010-5423

Chief
Benet Weapons Laboratory, CCAC
Armament Research, Development and Engineering Center
U.S. Army Armament, Munitions and Chemical Command
ATTN: SMCAR-CCB-TL
Watervliet, NY 12189-5000

Director
U.S. Army TRADOC Analysis Command-WSMR
ATTN: ATRC-WSS-R
White Sands Missile Range, NM 88002

GIDEP Operations Center
P.O. Box 8000
Corona, CA 91718-8000

Commander
U.S. Army Material Command
ATTN: AMCSG-H, Maj. Leggieri
5001 Eisenhower Ave
Alexandria, VA 22333-0001

Commander
U.S. Army Center for Health Promotion
and Preventive Medicine
ATTN: MCHB-DC-OHH, Maj. Mc Devitt
Cpt. Delk
D. Alberth
C. B. Weese
MCHB-DC-OFS, G. Braybrooke
MCHB-DC-TTE, W. McCain
MCHB-DS-HA, R. Gross
5158 Blackhawk Road
Aberdeen Proving Ground, MD 21010-5422

Commander
U.S. Army Test and Evaluation Command
ATTN: AMSTE-TM-O
AMSTE-TM-Safety Officer
Aberdeen Proving Ground, MD 21005-5055

Director
Aberdeen Test Center
ATTN: C. Wolff
R. Gibson
G. McKinny
Aberdeen Proving Ground, MD 21005-5055

Commander
Eglin Air Force Base
ATTN: WL/MNSE, D. Harrison
101 W. Eglin Boulevard
Eglin Air Force Base, FL 32542-6810

Commander
U.S. Army
Yuma Proving Ground
ATTN: STEYP-S, T. Brockington
Yuma, AZ 85365-9107

Commander
U.S. Army Medical Research Detachment
ATTN: MCMR-UWW, LTC R. E. Langford
2800 Q Street, Bldg 824
Wright-Patterson Air Force Base, OH 45433-7947

Headquarters
U. S. Army Medical Command
ATTN: MCHO-CL-W, E.G. Daxon
2050 Worth Rd.
Ft. Sam Houston, TX 78234-6000

Director
AFRRI
ATTN: T. Pellmar, RPT
E. J. Einsworth
Bethesda, MD 20889-5603